Journal of The Electrochemical Society

Editors' Choice—Improving Quality of EDMed Micro-Holes on Titanium via In Situ Electrochemical Post-processing: A Transient Simulation and Experimental Study

To cite this article: Ramver Singh *et al* 2024 *J. Electrochem. Soc.* **171** 013501

Journal of The Electrochemical Society, 2024 171 013501

Editors' Choice—Improving Quality of EDMed Micro-Holes on Titanium via In Situ Electrochemical Post-processing: A Transient Simulation and Experimental Study

Ramver Singh,[1,z] C. S. Rakurty,[2] Akshay Dvivedi,[1] and Pradeep Kumar[1]

[1]AMP Lab, Indian Institute of Technology Roorkee, Roorkee 247667, India
[2]The M. K. Morse Company, Canton, Ohio, United States of America

Electrical discharge micromachining (EDM) poses challenges to the fatigue-life performance of machined surfaces due to thermal damage, including recast layers, heat-affected zones, residual stress, micro-cracks, and pores. Existing literature proposes various ex situ post-processing techniques to mitigate these effects, albeit requiring separate facilities, leading to increased time and costs. This research involves an in situ sequential electrochemical post-processing (ECPP) technique to enhance the quality of EDMed micro-holes on titanium. The study develops an understanding of the evolution of overcutting during ECPP, conducting unique experiments that involve adjusting the initial radial interelectrode gap (utilizing in situ wire-electrical discharge grinding) and applied voltage. Additionally, an experimentally validated transient finite element method (FEM) model is developed, incorporating the passive film formation phenomenon for improved accuracy. Compared to EDM alone, the sequential EDM-ECPP approach produced micro-holes with superior surface integrity and form accuracy, completely eliminating thermal damage. Notably, surface roughness (Sa) was reduced by 80% after the ECPP. Increasing the voltage from 8 to 16 V or decreasing the gap from 60 to 20 μm rendered a larger overcut. This research's novelty lies in using a two-phase dielectric (water-air), effectively addressing dielectric and electrolyte cross-contamination issues, rendering it suitable for commercial applications.
 [DOI: 10.1149/1945-7111/ad19ec]

Manuscript submitted October 14, 2023; revised manuscript received December 11, 2023. Published January 10, 2024.

Titanium finds widespread use in high-strength, high-temperature applications like micro-nozzles, valves, filters, missile shields, howitzer barrels, turbocharger wheels, atomizers, and biomedical implants.[1] With tensile strengths of approximately 1000 MPa and significantly lower densities compared to nickel-based superalloys and generation 3 steels, it offers high specific strength, making it ideal for modern micro-engineering.[2] Titanium's exceptional corrosion resistance stems from the rapid formation of a tenacious oxide layer, the passive film, in oxygen-containing environments such as air or water.[3] Passive film forms quickly, even in newly developed cracks, minimizing the risk of further material degradation in corrosive conditions.[4]

Despite its favorable characteristics, besides high material costs, machining challenges pose the primary obstacle to the widespread use of titanium.[5] Titanium and its alloys fall under the category of "difficult-to-machine" materials. In conventional machining, thermophysical properties like thermal conductivity and heat capacity impact the tool-chip interface temperature and machining performance. Titanium's low heat-transfer characteristics lead to elevated interface temperatures, causing issues like tool wear, dimensional inaccuracies, and surface quality. To address this, non-conventional micromachining methods are preferred.

Non-contact micromachining techniques, commonly employed for fabricating miniaturized holes, encompass Electrochemical Machining (ECM)[6] and Electric Discharge Machining (EDM).[7,8] ECM operates on the principle of anodic dissolution, resulting in smooth surfaces without thermal damage, residual stresses, burrs, or tool wear. However, the challenge arises when machining materials like titanium and its alloys due to the formation of impervious and stable oxide films. ECM struggles with material removal due to the excellent corrosion resistance of titanium, and stray cutting becomes a significant concern.

On the other hand, EDM proves effective in producing accurate features.[9] Nevertheless, the thermal impact of EDM negatively affects the fatigue life of machined surfaces.[10] Thermal damages, including the recast layer, subsurface alterations (e.g., heat-affected zone and converted layer), metallurgical changes, and the presence of surface defects like micro-globules, crevices, burrs, and pores, all contribute to the deterioration of components exposed to fatigue loading conditions.[11] In addition to the thermal challenges, EDM yields rough surfaces due to repeated discrete spark discharges.[12,13] The higher roughness is believed to worsen the fatigue life of the machined surface, as these surfaces become common initiation sites for fatigue failure.[14] Hence, avoiding such surface irregularities is crucial.

Various post-machining methods, including abrasive flow finishing, magneto-rheological finishing, chemical-mechanical polishing, and others, are routinely employed to mitigate EDM-induced surface damage.[15] While these procedures enhance surface quality, they necessitate a separate facility, leading to increased time and cost. Additionally, their suitability for finishing intricate three-dimensional surfaces remains a subject of debate.

In response to these challenges, researchers have explored the concept of post-processing EDMed parts on the same machining setup. Masuzawa and Sakai (1983) pioneered this approach with a sequential electrochemical finishing operation, eliminating thermal damage in wire EDMed parts and later extending it to micro-nozzle fabrication.[16] Subsequently, research on the sequential approach gained momentum in the micro-domain. To create precise, smooth, and deformation-free flexural micro-hinges, Xiaowei et al. (1997) employed a combination of EDM with orbital motion and sequential ECM methods. They discovered that orbital motion during EDM produced a suitable "arc shape of subtle neck" without distortion, while a pulsed waveform during ECM ensured high accuracy through localized anodic dissolution.[17]

Hung et al. (2006) reduced crater markings on EDMed surfaces with "Electro-glo 300" electrolyte in phosphoric acid, achieving a decrease in Rmax from 2.11 μm to 0.69 μm for inner micro-hole surfaces,[18] despite associated environmental and safety concerns with acid-based electrolytes. Zeng et al. (2012) reported a sequential approach using micro-EDM for material removal and micro-ECM for finishing, both performed on the same machining setup with a common electrode but different working fluids for EDM and ECM.[19] Nevertheless, the issue of cross fluid contamination remains a prominent concern.

Some studies have used low conductivity de-ionized (DI) water as a bicharacter fluid since it can behave as a dielectric and a weak

[z]E-mail: ramver@iitb.ac.in

electrolyte in both processes. Nguyen et al. (2012) demonstrated a hybrid EDM and ECM method wherein both processes work simultaneously for machining and finishing the work material.[20] This method's working principle resembles that of the electrochemical arc machining proposed by,[21] with the exception that it employs a low resistivity DI water instead of electrolyte solution and involves spark discharges instead of self-sustaining arc discharges. Chung et al. (2009) explored a finishing procedure for improving the surface integrity of micro-EDMed holes by effectively using an electrochemical polishing effect during the ECM with low conductivity de-ionized water.[22] However, the formation of an oxide layer impedes the polishing action generated because of electrochemical reactions during the machining of commercial pure titanium (known to form a tenacious, inert oxide layer) with low conductivity de-ionized water. As a result, thermal damage and crater marks may remain on the machined surface. Recently, Meng et al. (2022)[23] and Ahmed et al. (2022)[24] investigated simultaneous machining with low-concentration electrolyte solutions. However, these studies did not provide specific insights into overcutting, leaving a notable gap in the research. It is important to note that the application of higher voltages in conjunction with electrolyte solutions to enhance polishing may lead to potential overcutting, especially given the reported Ra values within the range of 3 to 5 μm.[23]

The above-cited literature highlights that the simultaneous approach entails the application of rather high voltage to generate electrical discharges, leading to overcutting and large hole sizes or low-conductivity solutions that reduce overcutting but compromise material removal and polishing. To address this, the sequential execution of EDM and ECM processes on a single machining facility proves to be a more viable option. In a sequential approach, each process can be independently optimized, eliminating the restriction of compromises. This approach effectively mitigates overcutting, as the EDM or ECM parameters can be fine-tuned independently. For example, the EDM process can be optimized for efficient material removal (rough machining), while ECM can focus on surface finishing and dimensional accuracy. This results in precise hole dimensions and enhanced surface quality.

Nonetheless, it is important to note that the sequential approach does have a significant limitation, namely the potential for the two working fluids to contaminate one another. Indeed, the potential for the two working fluids to contaminate each other can significantly impact the performance of these machining operations and raise concerns regarding their industrial applicability. This issue must be effectively addressed to maintain the viability of the process.

The novelty of this research lies in the use of a two-phase (water in air) dielectric fluid for near-dry EDM operation. This approach effectively addresses the concerns of fluid contamination. Because the trace amount of residual water on the work surface is not a problem as used electrolyte solution is also water-based, distinguishing this method from conventional approaches, which use EDM oil as the dielectric.

In this research, near-dry EDM is used to make initial holes, and ECM is used as post-machining processing to reduce surface roughness, dissolve heat damages, and repair form imperfections caused by the EDM operation. To expound on the evolution of overcutting in micromachining, we conducted a unique experiment. We adjusted the initial radial inter-electrode gap (IR-IEG, the shortest radial gap between the hole periphery and the tool periphery before ECPP begins) by reducing the tool diameter through in situ wire-electrical discharge grinding (wire-EDG). This allowed us to explore and understand its effect on the process, providing valuable insights into addressing overcutting. Furthermore, a transient FEM simulation model with deformed geometry has been developed to accurately predict the time-dependent hole profile evolution during the ECPP phase of the sequential process by considering the creation of an inert oxide layer in the passivating electrolyte solution, such as $NaNO_3$. The simulation model couples electric current distribution with deformed geometry. The simulation model was validated using

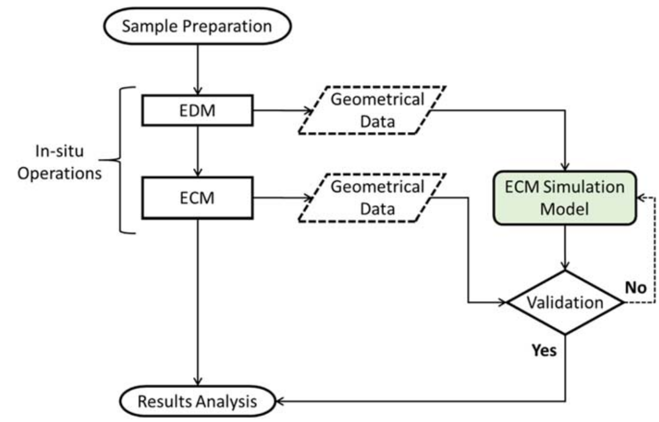

Figure 1. A flow chart illustrating the investigation procedure.

hole profiles from varied ECPP durations. This study uses the full factorial technique to clarify how process parameters such as IR-IEG and applied voltage affect response characteristics. Energy dispersive X-ray spectroscopy, scanning electron microscopy (SEM), and X-ray photoelectron spectroscopy (XPS) were used to analyze treated surfaces.

Research Methodology

Overview.—Figure 1 illustrates the investigation scheme flowchart. Initial micro-holes were produced using the EDM process, and data from geometric analysis served as the basis for constructing a finite-element method (FEM) based numerical simulation model for the subsequent electrochemical post-processing (ECPP) stage. The model was subsequently validated through comparison with experimental ECPP data, followed by a thorough analysis of the results.

The numerical simulations were used in conjunction with experimental investigations to simulate the transient behavior of material dissolution and evaluate the effects of changing input parameters, more efficiently and precisely than experimental methods alone. Because an experimentally verified simulation model can predict a multi-physics problem more quickly than conducting experiments alone, thereby it assists in gaining a better understanding of the process in a cost-effective manner.

Work materials and experimental facility.—Workpiece samples measuring 10 mm × 20 mm were cut from a 2 mm sheet of commercially pure titanium (Grade 2). A tabletop-type miniature micro-EDM machine (model: Hyper-15; make: Sinergy Nano Systems, India), equipped with a wire-EDG attachment for on-site fabrication of micro-sized tools, was modified to conduct this investigation. The modification included mounting near-dry dielectric flow and ECPP attachments onto the EDM machine. A three-dimensional (3D) schematic model of the experimental facility is depicted in Fig. 2.

A three-axis positioning system, which provided a linear resolution of approximately 0.1 μm, facilitated tool movement in both the vertical axis (Z-axis) and the horizontal (XY) plane for the worktable.[25] In EDM for fabricating initial holes, the servo-mechanism-equipped vertical axis allowed the tool to move adaptively, ensuring the desired IEG value in the longitudinal direction as the tool advanced.[26]

In the context of ECM, controlling and maintaining a specific IEG value was crucial. Various strategies for controlling tool motion to achieve the desired IEG values in the ECM process were suggested in the literature.[27] However, in performing the ECPP operation for this study, motion control in both the longitudinal (Z-axis) and radial (X or Y axes) directions was deemed unnecessary. This decision was rooted in the tool's non-fed approach; rather than being fed, it was precisely plunged into the initial hole at a predetermined Z-axis coordinate corresponding to the hole depth,

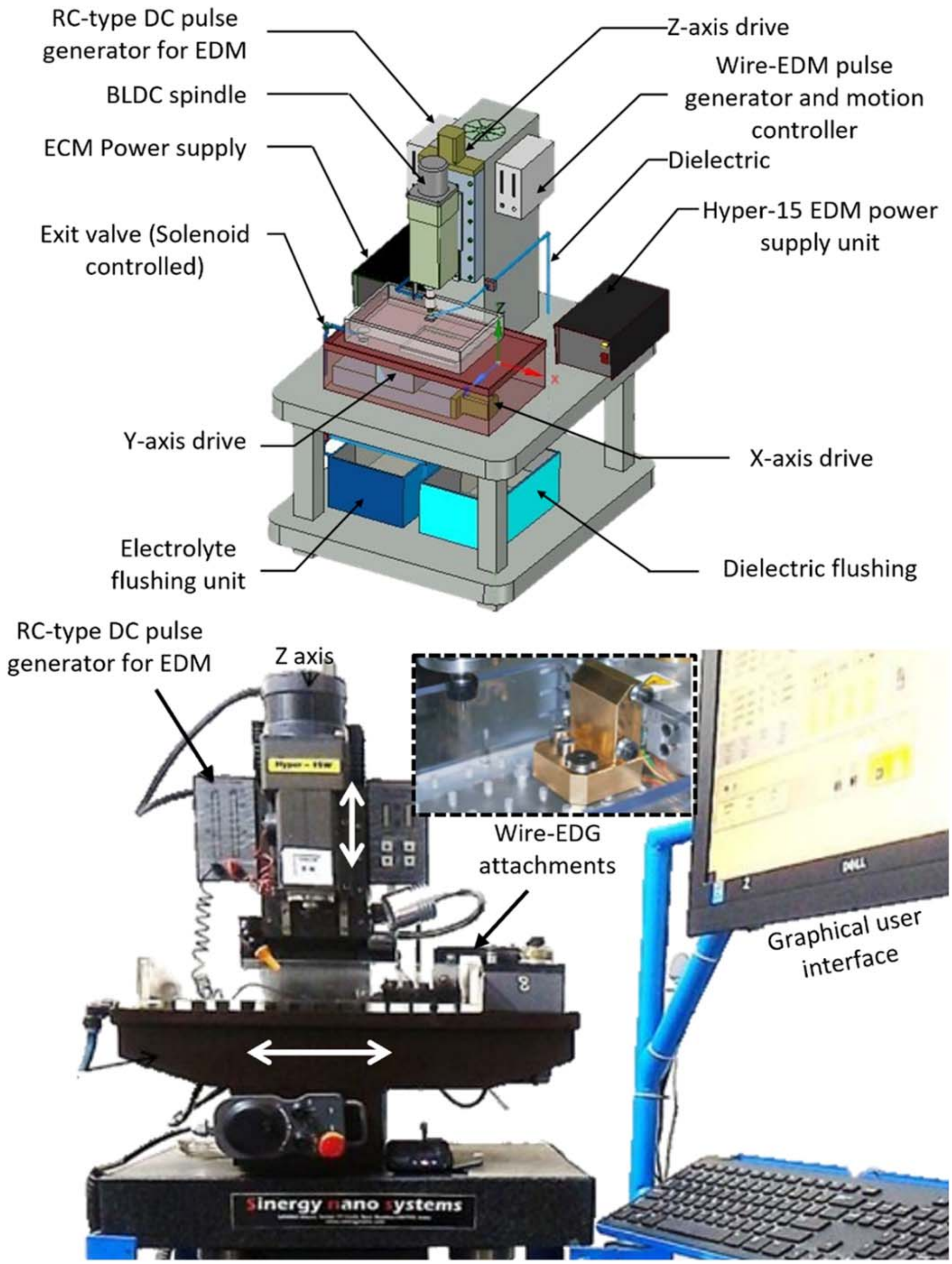

Figure 2. Images depicting the experimental setup and an image of the modified EDM machine equipped with on-machine tool fabrication capabilities using a wire-EDM attachment,[30] as displayed in the inset.

maintaining a stationary position thereafter. Nonetheless, an active implementation of wire-EDG ensued to systematically reduce the tool diameter post-initial hole fabrication. This deliberate action aimed to assess the effect of varying the IR-IEG on the performance of ECPP operation.

The modified facility employed two distinct power suppliers for sequential EDM and Electrochemical post-processing operations. The EDM operation utilized an RC-type pulsed direct current (DC) power supply that could deliver pulsed electrical signals up to 220 V. The discharge energy was adjustable by selecting from different capacitors with capacitance values of 0 pF (only stray capacitance), 10 pF, 100 pF, 1000 pF, and 10000 pF. On the other hand, the ECPP operation used a transistor-based DC power supply unit that could supply up to 30 V with a limiting current of 2 A. Both power supply units were equipped with short circuit protection to prevent damage resulting from inadvertent contact between tools and work material. An electronic switch facilitated the selection between these power inputs.

The near-dry dielectric flow attachment was employed to generate a two-phase mixture of air and water, which was subsequently introduced into the machining zone to aid in debris removal during the near-dry EDM process. Further details about this near-dry system can be found elsewhere.[28,29] For the near-dry EDM, air was supplied at 50 psi and water consumption was 6 ml min^{-1}. At these parameters, the flow of dielectric mixture was consistent.

The ECPP attachment included a DC power supply and had provisions for electrolyte filtration and circulation. The recirculation of the fresh electrolyte solution was achieved using a diaphragm

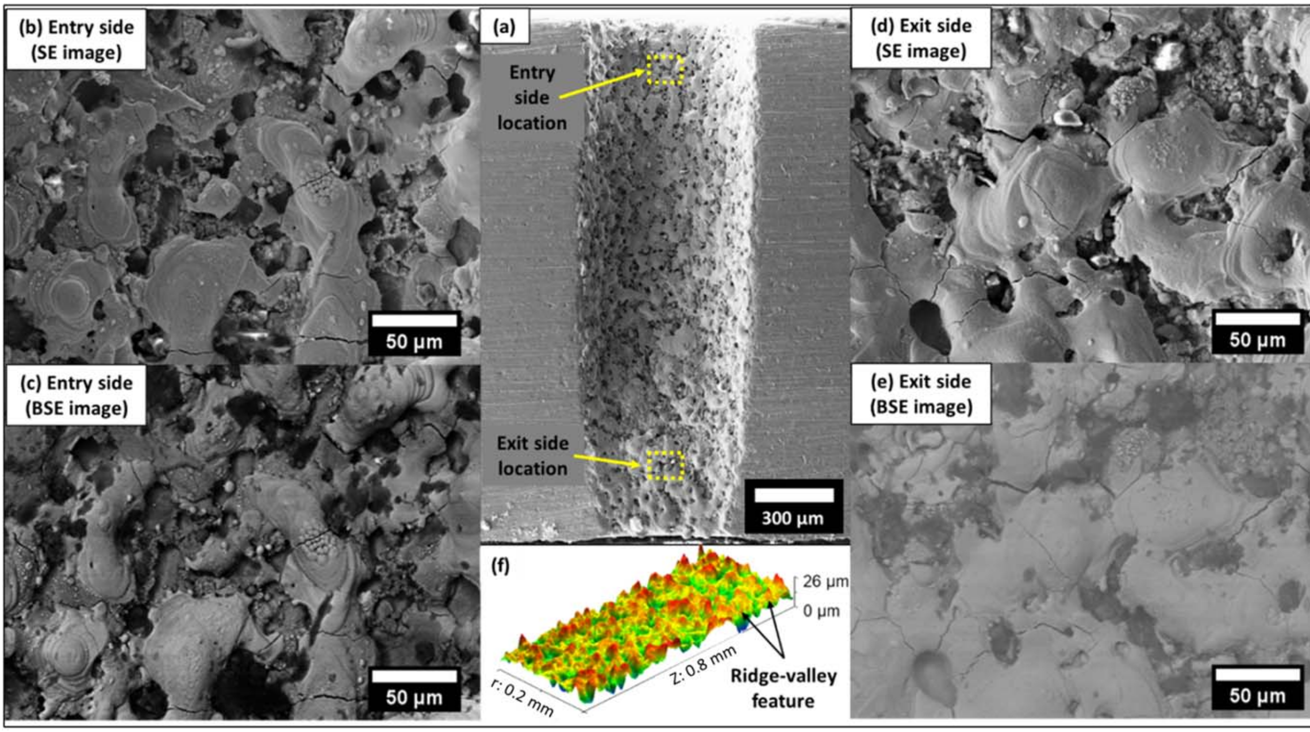

Figure 3. The typical FE-SEM images of the cross-sectioned EDMed initial hole (a), and (b)–(e) the surface morphology of the initial EDMed holes at marked locations on entry and exit sides; (f) the axonometric images depicting the surface morphology of the initial holes.

Table I. A summary of the ECPP experimental parameters.

S. No.	Parameters	Description/values
1.	Electrolyte solution	aqueous $NaNO_3$
2.	Concentration	0.5 M
3.	ECPP duration	15 s
4.	Applied voltage	8, 10, 12, 14, 16 V
5.	Initial radial IEG	20, 40, 60 μm

pump, with solenoid valves controlling the electrolyte flow. A 0.5 M $NaNO_3$ aqueous solution served as the preferred electrolyte over acids or NaCl for multiple reasons. Acids would have potentially posed corrosion risks and safety concerns, while NaCl would have enlarged hole sizes due to the aggressive chloride ion pitting. These alternatives did not align with our objectives of addressing EDM-related issues and maintaining eco-friendliness.

The tool holder carried a cylindrical-shaped tungsten rod of roughly 800 μm in diameter. The required nominal tool diameter was around 500 μm. Hence, the tool diameter was reduced on-site at the same EDM machine using the wire-EDG attachment. Additional details on the wire-EDG procedure can be found in Kumar and Singh.[30,31] The wire-EDG feature played a crucial role in preventing tool-mounting errors. More importantly, in situ wire-EDG was employed to examine the effect of altering the IR-IEG from 20 μm to 40 μm or 60 μm by reducing the tool diameter from 500 μm to 480 μm or 460 μm.

The term "in situ" in this work highlights that the ECPP of micro-holes, initially created by EDM, was directly performed "on-site" using the same EDM machine. This emphasizes that the EDM, wire-EDG, and ECPP operations were executed on the same machine without dismounting or disturbing either the tool or workpiece. This method eradicates tool mounting errors and minimizes setup time between operations, ultimately improving the repeatability and productivity of the process.

Experimental procedure and details.—A total of 76, calculated as $(1 + 3 + 15) \times 4$, initial holes were machined using EDM under the same parametric setting of voltage (120 V), capacitance (10000 pF) with positive workpiece polarity. Four repetitions were performed for each experiment. We chose the EDM parameters such as voltage (120 V) and capacitance (10,000 pF) to enable faster hole drilling under rough machining conditions. These parameters increase spark discharge energy, leading to faster machining speed but rougher surface characteristics.[32] Out of these 76 holes, four holes were utilized to characterize the geometrical and surface characteristics of the initial EDMed holes. Twelve holes were allocated for the experimental validation of the ECPP simulation model, while the remaining 60 holes were dedicated to parametric investigation. Before longitudinally cross-sectioning these holes for surface analysis, their diameters were measured using the SEM microscope. The average values of these measurements were considered for further analysis during the evaluation of ECPP operation.

Before ECPP operation, to maintain tool uniformity for each experiment, the worn length of the tool was cut off using wire-EDG. The experimental investigations were performed by following the full factorial approach, controlling two key parameters: applied voltage and IR-IEG. We adjusted IR-IEG by reducing the tool diameter through wire-EDG, as detailed previously. Table I displaying the parameters employed for ECPP operation. The preliminary ECPP test results indicated that applying voltages less than 8 V or an initial radial IEG (IR-IEG) broader than 80 μm did not produce sufficient anodic dissolution for achieving a recast layer-free hole surface. Conversely, excessive material dissolution and high overcut occurred with voltages that were too high (16 V) or IR-IEG values narrower than 20 μm. Consequently, the feasible range of process parameters studied in this work includes an applied voltage range of 8 to 16 V and an IR-IEG of 20 μm to 60 μm.

Characterization techniques.—The quality characteristics of the micro-holes, such as the radial hole over-cut (HOC), mean roughness (Sa), and recast layer thickness, were characterized before and after the ECPP operation. An image processing software program

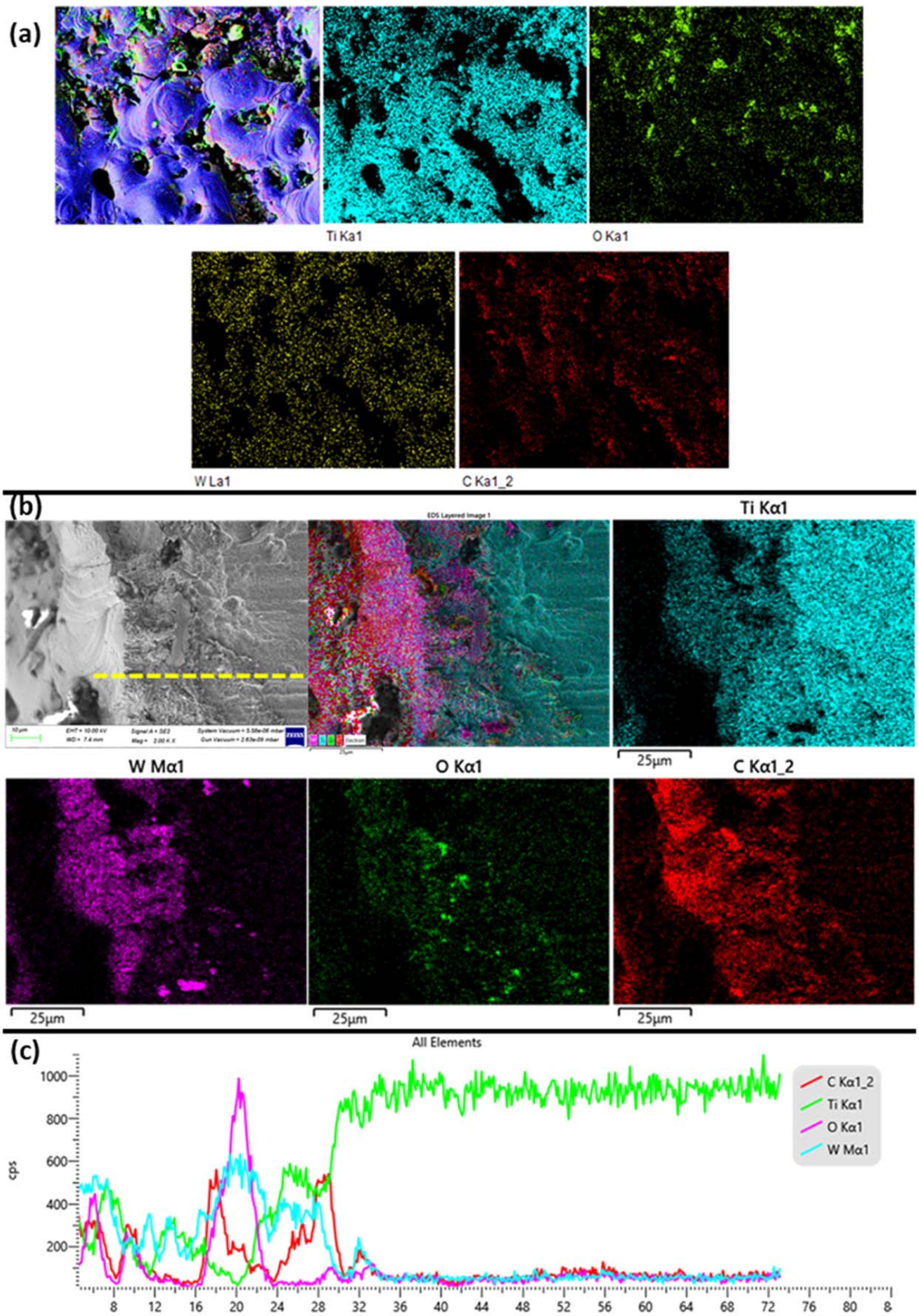

Figure 4. The representative EDX elemental distribution analyses for titanium, tungsten, oxygen, and carbon: (a) over the surface of the initial EDMed holes, (b) on the cross-section of the recast layer exposed after chemical etching in Kroll's reagent, and (c) line scan diagram displaying the elemental variation across the marked line in figure (b).

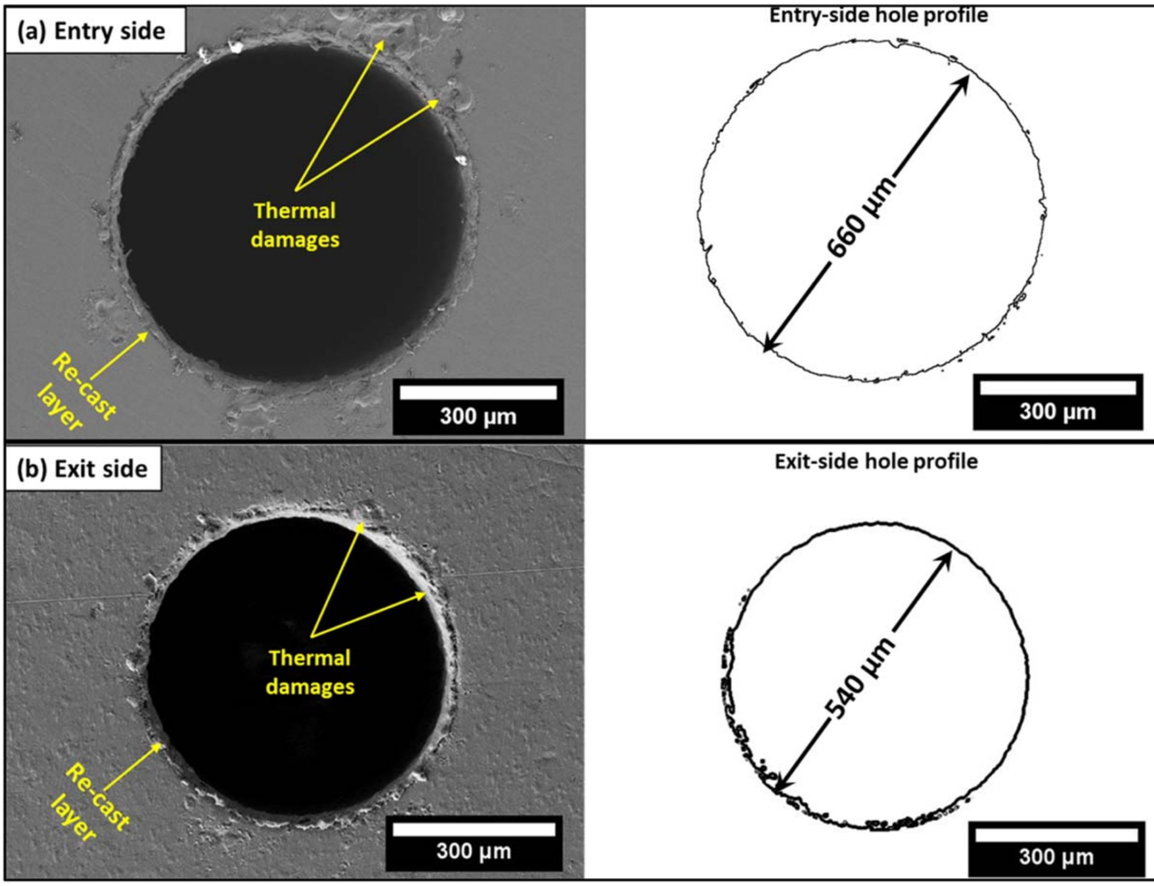

Figure 5. The representative FE-SEM micrographs depict the profile of the initial EDMed holes viewed from tool's (a) entry and (b) exit sides.

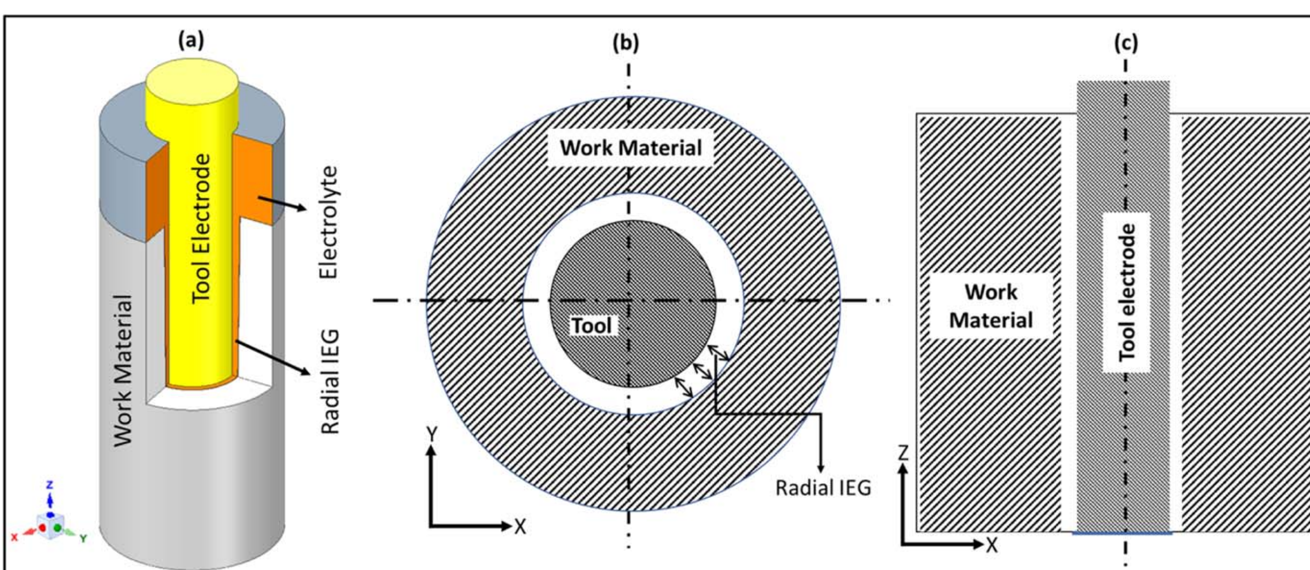

Figure 6. Schematic images display the developed geometrical model of the initial holes shown (a) in three-dimensional (3D) trimetric view, (b) in radial cross-sectional view, and (c) in longitudinal cross-sectional view.

(ImageJ) was employed to obtain the geometrical features. The average values of radii were calculated. These values were eventually used for two purposes: first, as the input data to draw the shape of the initial micro-holes during the numerical simulation investigation; and second, to assess the effect of ECPP operation on hole over-cut (HOC). The HOC is calculated from Eq. 1.

$$\begin{aligned} &Hole \quad overcut, HOC(\mu m) \\ &= Hole \quad radius(\mu m) - tool \quad radius(\mu m) \end{aligned} \quad [1]$$

To examine the change in the surface morphology, the sample holes were sectioned longitudinally and then polished following the

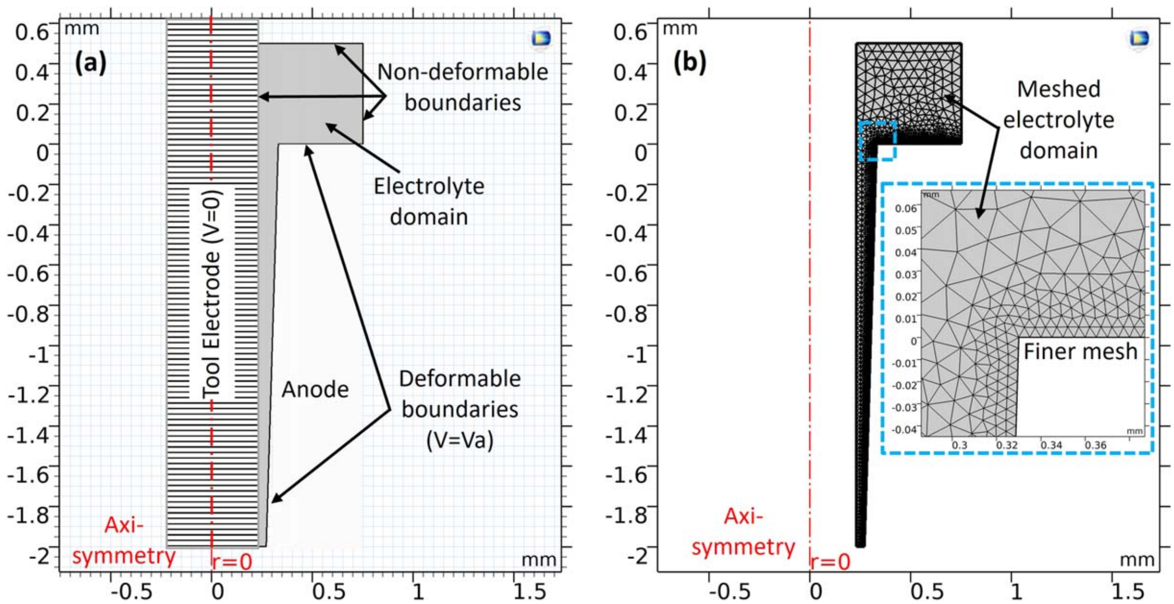

Figure 7. Images representing (a) the axisymmetric geometry model of the electrolyte domain, tool electrode, and anode; (b) the meshed geometry of the model, inset zoom-in view of the mesh depicting the triangular-shaped mesh elements having higher mesh density nearby the initial electrolyte-work material interface.

procedure mentioned above. The quantitative roughness values were obtained using an optical profilometer working on the principle of white light interferometry (Model: Sigma; Make: Rtec Instruments). A 10x objective lens was employed to examine the cross-sectional hole surface, with a cutoff length of 0.8 mm. After subtracting the second-order polynomial background to account for the curvature of the cylindrical hole, Sa values were determined. A scanning electron microscope (SEM, make: Carl-Zeiss) was used to examine the surface morphology of the micro-holes qualitatively. The Kroll's Reagent solution has been used to reveal the recast layer. The thickness of the recast layer was obtained through image processing of the SEM micrographs of the recast layers. Similarly, the surface characteristics of micro-holes after the ECPP operation were investigated.

Results and Discussion

This section is divided into four segments. The first subsection examines the initial EDMed micro-holes. The second subsection, which employs geometrical data gathered in the first, builds and validates the transient model to predict hole profile evolution during ECPP operation of the sequential approach. The third subsection deals with experimental and numerical analyses of process performance and parameters. The last subsection details the mechanics of the proposed sequential ECPP approach.

Examining the initial EDMed micro-holes.— *Cross-sectional analysis.*—Cross-sectional study characterized the initial holes' surface morphology and recast layer. Figures 3b–3e show typical FE-SEM micrographs of initial EDMed hole surface morphology at marked entry and exit sites. The holes' top and bottom ends were examined morphologically. The top end was rougher than the bottom. Reattachment of particles to the machined surface and aberrant radial IEG discharge might cause it. Both cause rougher, irregular surface morphology. These events are more likely to occur at the top end, hence, EDMed hole surface morphology varies. The initial holes exhibited crater markings and splatters. According to the literature,[13] the EDM process involves sparks discharging to remove a small amount of material by melting and vaporizing material from the surface, leading to the formation of micro-craters.

Figure 3f shows axonometric photographs of initial hole surface morphology. Processing raw white light interferometer (WLI) data with open-source software yielded the mean roughness (Sa) (Gwydion). Roughness characteristics were calculated for a scan area of 0.2 mm × 0.8 mm. Mean roughness (Sa) was 3.01 ± 0.17 μm. Figure 3 shows the surface had ridge-valley-like structures.

The SEM analysis revealed the presence of recast layer (RCL). Figure 4 shows typical FE-SEM images of the RCL. EDS area mapping examined recast layer element distribution. Carbon, tungsten, and oxygen were incorporated into the RCL. Hydrocarbon-based-EDM oil breakdown may embed carbon in the RCL. Tungsten transfers material from the tool electrode during spark discharge. The line scan graph in Fig. 4c shows that carbon, oxygen, and tungsten concentrations are lowest towards the bulk material area. Image analysis showed that the original holes had 29.83 ± 4.25 μm RCL thickness.

Geometrical characterization.—Figure 5 shows the tool's entrance and exit FE-SEM micrographs of the initial EDMed holes' profiles. All sides of the original EDMed holes have thermal degradation, including the recast layer. Image processing software (ImageJ) assessed the initial holes' top (entry) and bottom (exit) radii (i.e., $r_{t,i}$ and $r_{b,i}$) averaged 330 μm and 270 μm. Spark discharges

Table II. The details of different factors utilized in the simulation model.

S. No.	Parameter name	Values
1.	Density, ρ_{Anode}	4.5 g cm^{-3}
2.	Relative atomic mass of anode, M_{Anode}	47.867
3.	Valency, z	4
4.	Minimum current density, J_{min}	30 A cm^{-2}
5.	Electrical conductivity of the electrolyte solution, σ	4.2434 S m^{-1}

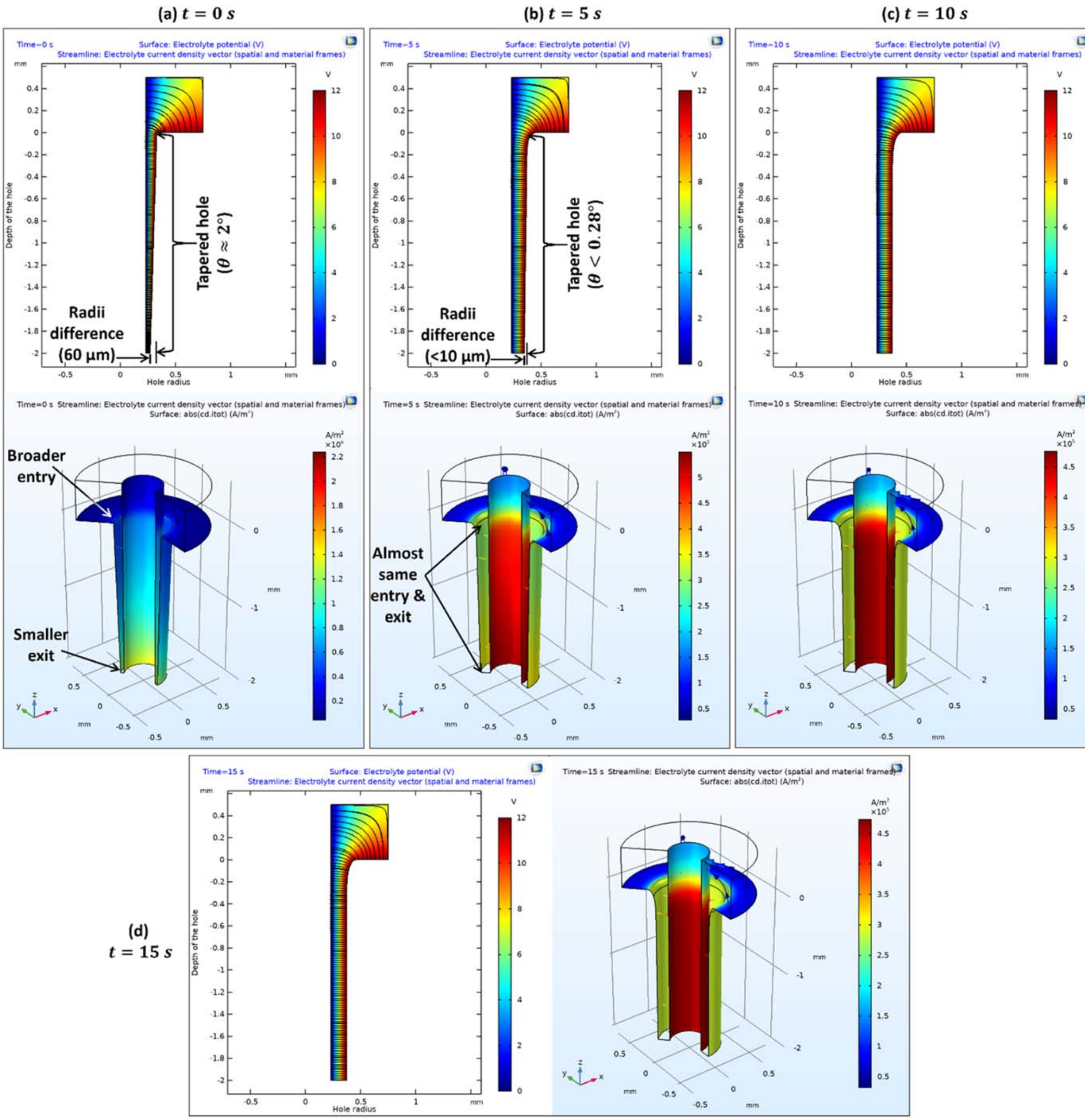

Figure 8. Images depicting the transient distributions of electrolyte potential and related electrolyte current density during ECPP operation for an applied voltage of 12 V and an IR-IEG of 40 μm at four different time steps: (a) t = 0 s, (b) t = 5 s, (c) t = 10 s, and (d) t = 15 s.

diminish tool diameters at the frontal face during EDM, causing a difference in radii. Hole taperness is undesirable. Post-processing must correct it. As a result, the geometric model of the initial holes featured tapered walls at an angle of approximately 2 degrees.

Developing a transient numerical model of in situ ECPP hole profile evolution.—The in situ ECPP operation was simulated numerically using a commercially available software package (COMSOL Multiphysics^{TM}). The numerical simulation model was developed by coupling the electric current distribution with deformed geometry to predict the evolution of the hole profile during the ECPP operation. The model geometry was drawn using the data obtained from the geometrical characterization of the initial micro-holes machined through the EDM process. The model was assumed to be axisymmetric about the holes' longitudinal axis. It consisted of three domains: electrolyte, tool electrode (cathode), and work material (anode). The initial holes had taper-ness.

Figure 6 depicts the three-dimensional axis-symmetric model with initial hole schematics. The model is virtually symmetrical along the cylindrical tool and machined hole longitudinal axis, as illustrated in the cross-sectional images. Hence, the three-dimensional electrolyte domain has been simulated using the two-dimensional (2D) axisymmetric approach (3D). The axisymmetric method estimates 3D domain solutions efficiently and correctly.

Figure 7a displays the axisymmetric geometrical model of the electrolyte domain. The free triangular elements with higher mesh density near the initial electrolyte-work material interface were used to discretize the domain. The meshing was generated using the

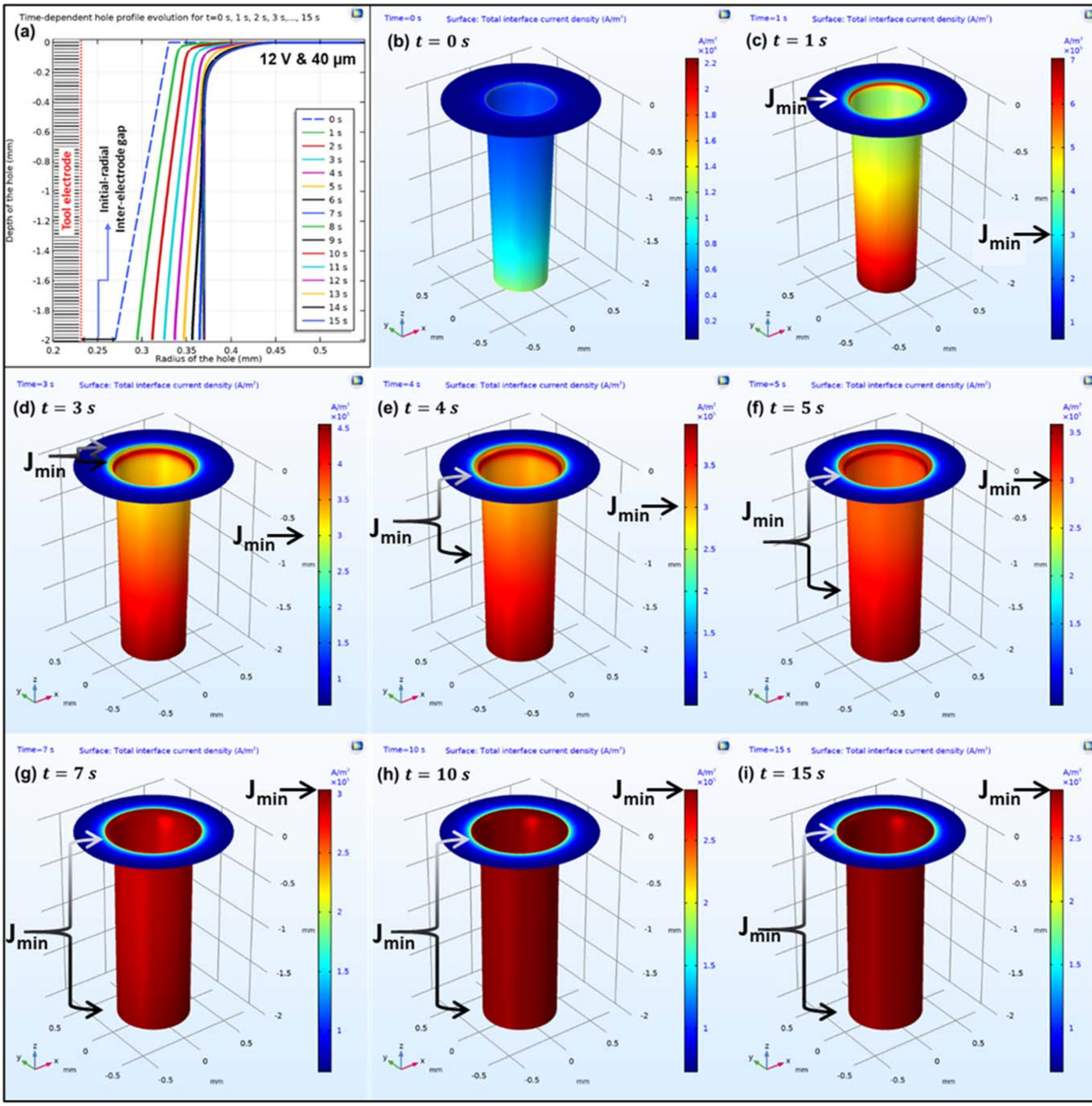

Figure 9. Images showing hole profile change. (a) A line graph showing the hole profile's radial cross-section over ECPP time. ECPP operation's 3D micro-hole shape development and total current density distribution at the hole surface: (b) 0 s, (c) 1 s, (d) 3 s, (e) 4 s, (f) 5 s, (g) 7 s, (h) 10 s, and (i) 15 s.

automatic mesh generator. The maximum element size near the anode was approximately 5 μm, while it increased to 55 μm for the electrolyte domain located far from the anode. The curvature factor stood at 0.25, and the maximum element growth rate was 1.25. Figure 7b depicts the meshed geometry of the model. The COMSOL 5.4 Multiphysics software was used to solve the model with deformed geometry. The following sub-sections provide more information about the governing equations, assumptions, and initial boundary conditions.

Material dissolution governing equations.—According to Faraday's law, the volume of material dissolved during the ECM is estimated from the Eq. 2,

$$V_{vol} = \eta(J)\cdot\frac{M_a}{\rho \times z \times F}\cdot I\cdot t \quad [2]$$

where, V_{vol} is the volumetric anodic dissolution, I is current, t is the ECPP duration, M_a is the anode's atomic mass, ρ is the density, z is the valency of the anode, and F is the Faraday's constant, and is equal to 96,485 (C/mol). The dissolution efficiency, $\eta(J)$, the term was introduced to take account of the discrepancy in the theoretical and experimental values of V_{vol}. It is a function of local current density.

The linear anodic dissolution rate is more appropriate than the volumetric dissolution rate to simulate the evolution of the anode profile during the electrochemical micromachining process.[33] Thereby, the rate of anodic dissolution in the normal direction

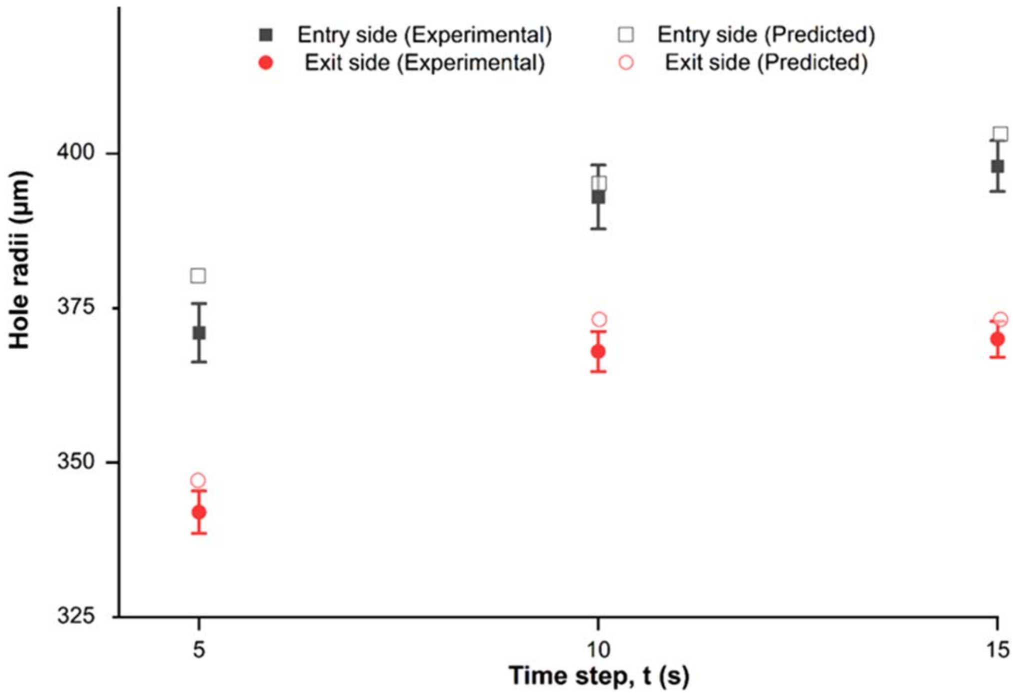

Figure 10. Image showing hole radii from numerical modelling and validation studies for ECPP time durations of 5, 10, and 15 s.

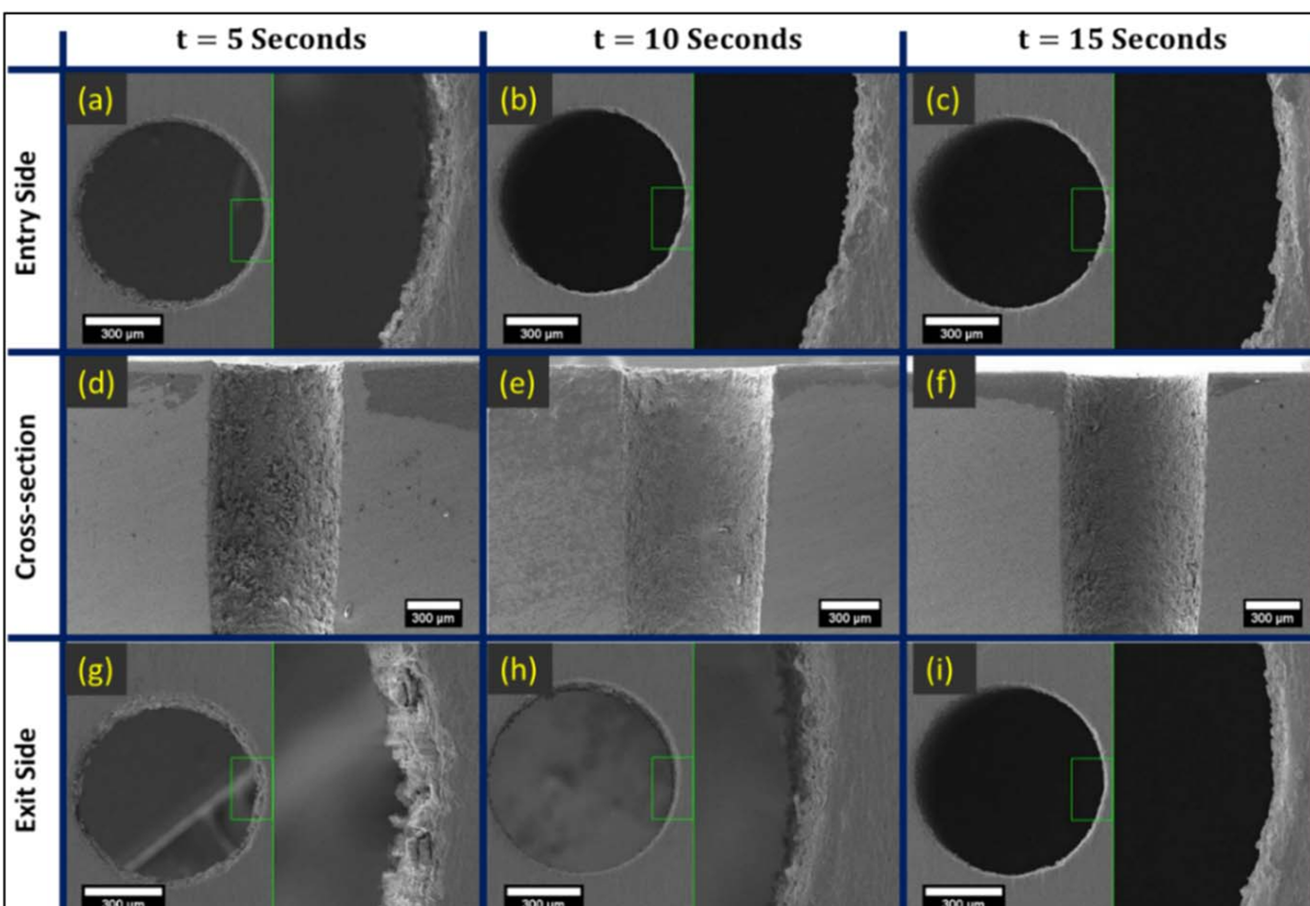

Figure 11. The typical FE-SEM images display the radial hole profiles at the entry side (a)–(c), the longitudinal cross-sectional hole profile (d)–(e), and the radial hole profiles at the exit side (g)–(i). The scale bar is 300 μm.

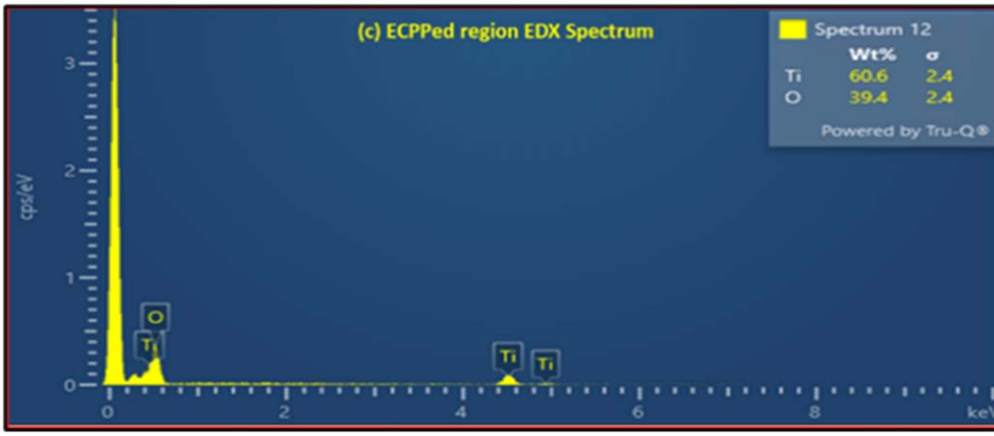

Figure 12. The EDS spectrum of the ECPPed region.

($\vec{V_{fn}}$ which enunciates the machining speed in μm/s) can be given by Eq. 3.

$$\vec{V_{fn}} = \eta(J)\cdot\frac{M_a}{\rho \times z \times F}\cdot\frac{I}{A} = \eta(J)\cdot\frac{M_a}{\rho \times z \times F}\cdot\vec{J_n} \quad [3]$$

Where, $\vec{J_n}$ is the current density in the normal direction.

Assumptions and initial boundary conditions.—The ECPP operation was modeled in view of the following assumptions:

• Only the electrolyte domain was considered as the region of investigation. The potential gradients developed inside both electrodes were neglected because the electrical conductivities of both electrodes (made up of metals) are considerably higher than that of the electrolyte solution. Thus, the primary current distribution was assumed to be applicable as the activation potentials of both electrodes were neglected.

• The concentration, thermal gradients, and material transport phenomena were neglected because the cleaned electrolyte was supplied continuously into the machining zone. As a result, the electrolyte conductivity was assumed to be constant throughout the region of investigation for a given concentration of electrolyte solution. Hence, Laplace's equation was assumed to be applicable. Eq. 4 (Laplace's equation in polar coordinates frame of a reference system) was used to calculate the distribution of electrolyte potential (∅) inside the radial IEG formed between the cylindrical tool and the peripheral surface of the initial hole.

$$\nabla^2\varnothing = \frac{\partial^2\varnothing}{\partial r^2} + \frac{1}{r} \times \frac{\partial\varnothing}{\partial r} + \frac{1}{r^2} \times \frac{\partial^2\varnothing}{\partial\theta^2} = 0 \quad [4]$$

• At the anode, no other reactions except the metal dissolution reaction ($Ti \rightarrow Ti^{4+} + 4e$) take place. Further, the work material was removed only through anodic dissolution.

• The surfaces of both electrodes were assumed to be equipotential surfaces. The tool electrode was assumed to be at 0 V (i.e., grounded). Whereas the work material was set to the applied voltage (V_a).

• The tool electrode axis was defined as axisymmetric, and the tool surface (cathode) was considered as a non-deformable boundary with zero normal displacement. Further, the work material (anode) was geometrically deformable in the normal direction.

• During the ECM of titanium or its alloys with a passivating electrolyte solution, such as the aqueous solution of sodium nitrate, a region of low current densities ($\leqslant J_{min}$) exists, whereby the phenomenon of anodic dissolution does not occur due to the creation of the inert, anodic oxide layer. Based on the literature, the value of J_{min} was assumed to equal 30 A cm^{-2}. Therefore, the binary conditions expressed by Eq. 5 were used to consider this fact.

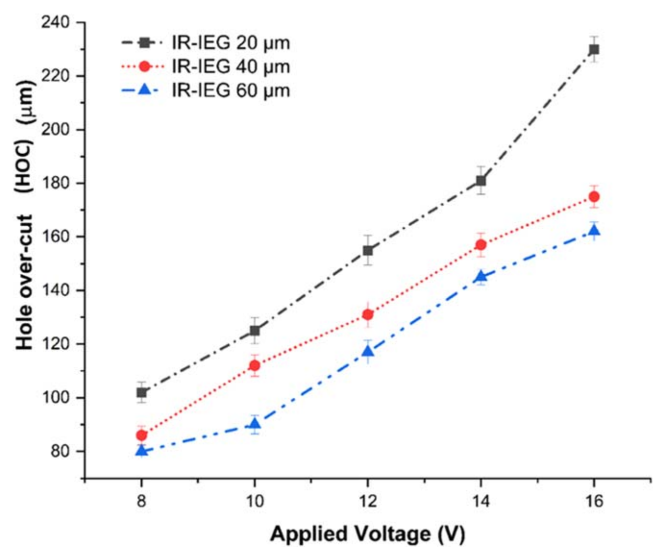

Figure 13. The effect on hole over-cut (HOC) values when changing the applied voltage from 8 V to 16 V for three distinct initial radial interelectrode gap (IR-IEG) widths (i.e., 20 μm, 40 μm, and 60 μm).

$$\eta(J) = \begin{cases} 1 \; for \;\; J > J_{\min} \\ 0 \; for \;\; J \leqslant J_{\min} \end{cases} \quad [5]$$

We assumed a current efficiency of 100% due to the presence of microcracks and pores on the recast layer, resulting in a lower corrosion-resistance of the EDMed surface, eventually leading to higher dissolution rate compared to the pristine surface.[34]

• Table II summarizes the details of various factors utilized in the simulation model.

Figure 8 displays the transient distributions of electrolyte potential and related electrolyte current density during ECPP operation at four distinct time steps (t = 0 s, 5 s, 10 s, and 15 s) with an applied voltage of 12 V and an IR-IEG of 40 μm. At the start of the ECPP operation, i.e., at t = 0 s, the largest electrolyte current density (about 140 A cm^{-2}) occurs on the exit side of the hole, whereas the lowest (approximately 40 A cm^{-2}) exists near the entry side of the hole, as shown in Fig. 8a. The electrolyte potential distribution across the radial IEG keeps changing because the IR-IEG enlarges with progress in ECPP time.

Figure 9 shows the shape evolution of the initial holes during ECPP operation and the related electric field intensity distribution with a 12 V applied voltage and a 40 μm initial radial interelectrode

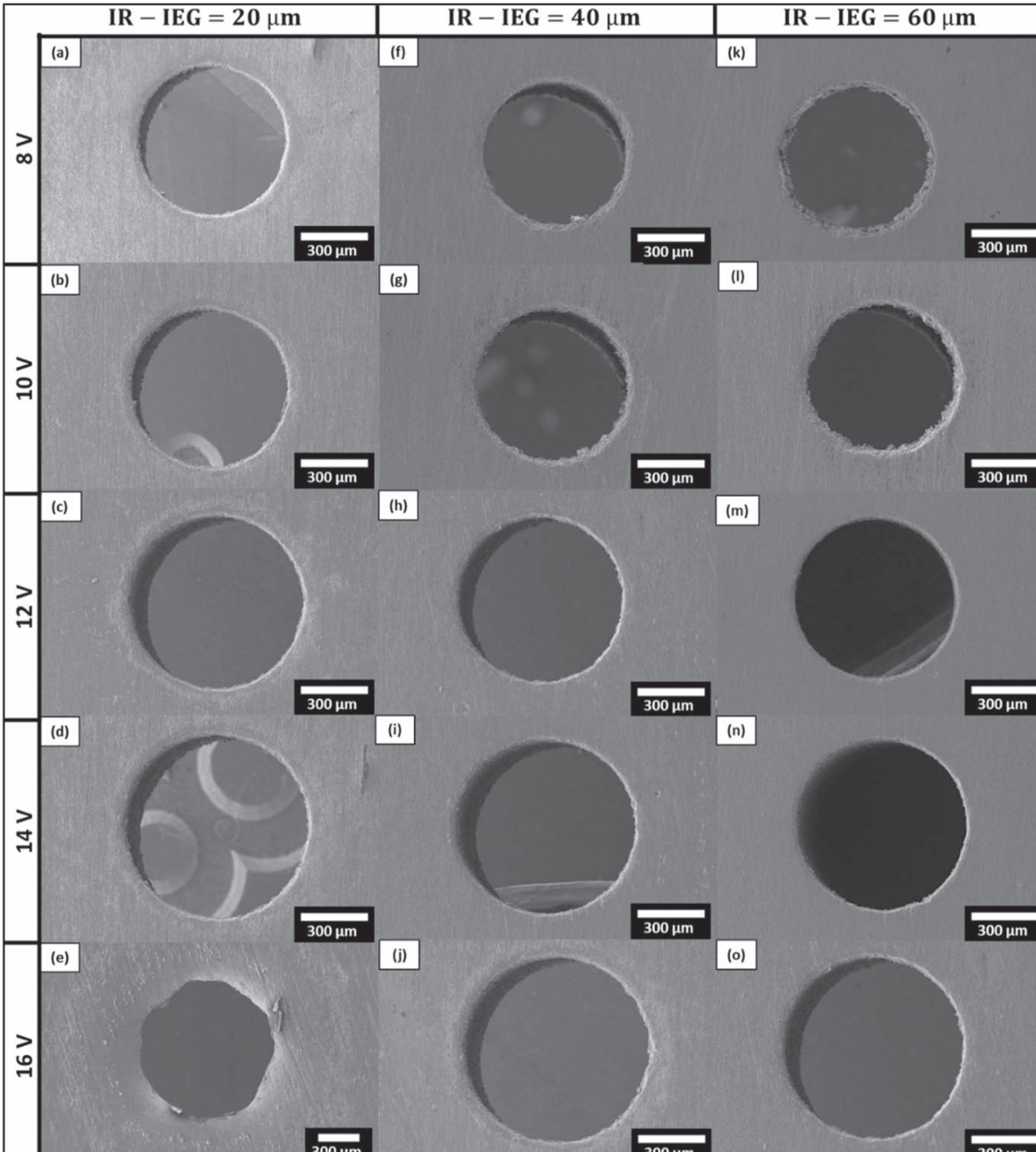

Figure 14. The typical FE-SEM micrographs display the radial hole cross-sections of the micro-holes. The micrographs arranged from left to right have the initial radial inter-electrode gap (IR-IEG) distance of 20 μm, 40 μm, and 60 μm, respectively. The micrographs arranged in rows from top to bottom represent increasing applied voltages from 8 V, 10, 12 V, 14 V, and 16 V. The scale bars are 300 μm.

gap (IR-IEG). In Fig. 9a, the dotted blue line depicts the initial hole profile before ECPP operation. On the other hand, the green, red, and other color lines depict the evolutionary hole profile at t = 1 s, 2 s, and so on as predicted by the numerical simulation model created under the afore-stated assumptions and boundary conditions. The three-dimensional geometries of the holes shown in Figs. 9b–9i were formed by rotating these radial cross-sectional profiles along the tool and hole's longitudinal axis.

Since the initial hole had a taper, a variation in the radial IEG existed over the longitudinal distance of the hole. It means that if the radial IEG values at the entry and exit ends were not the same, the anodic dissolution rate would not be the same either. In fact, the material dissolution rate is inversely proportional to the value of radial IEG as per Faraday's law and Ohm's law. A higher anodic dissolution rate is predicted at the exit end of the hole because there exists a higher current density owing to a narrower radial IEG than at

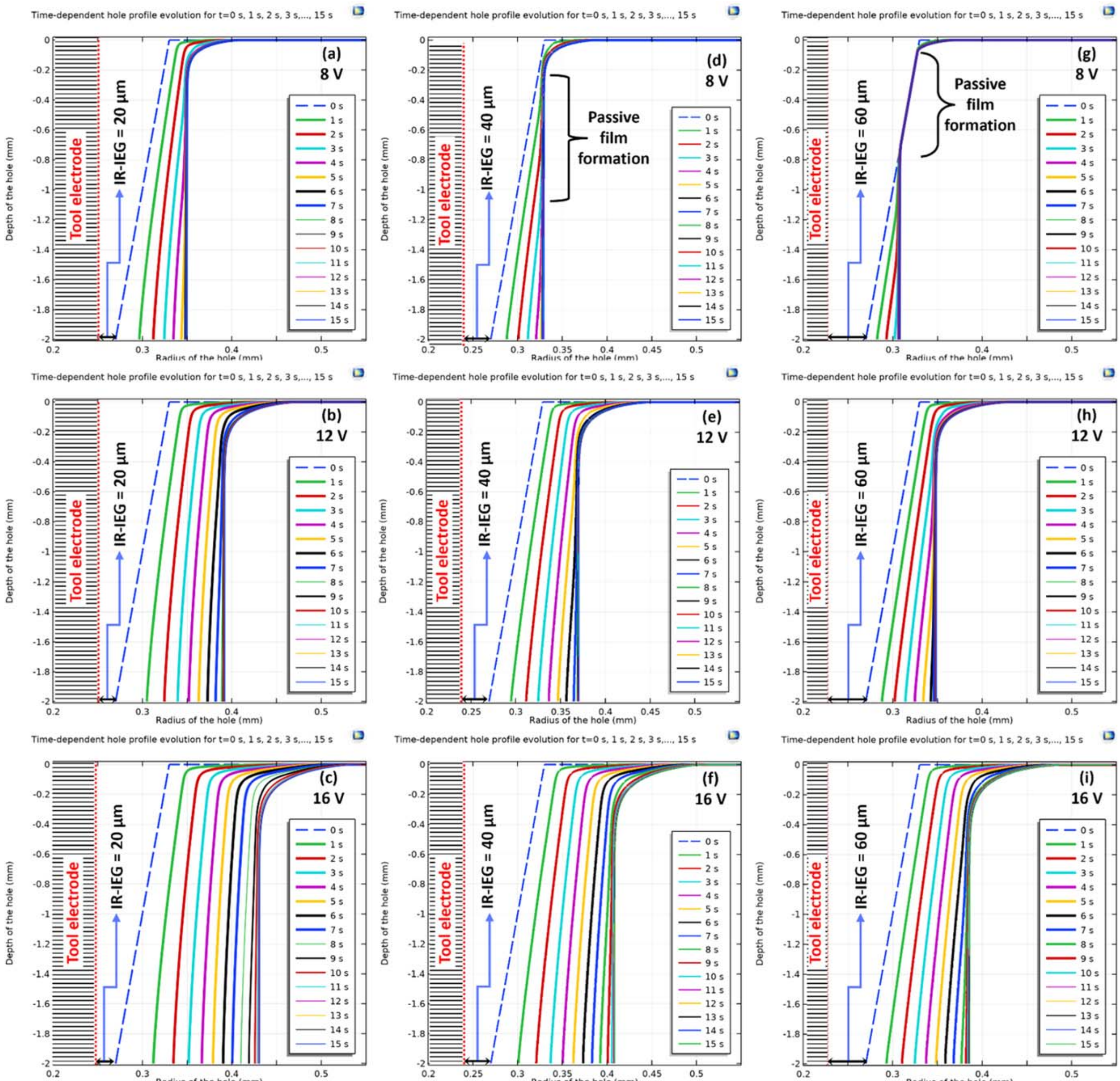

Figure 15. Radial cross-sectional line graphs demonstrating the time-dependent evolution of the hole profile predicted from numerical simulations for three applied voltage values: 8 V (a), (d), and (g), 12 V (b), (e), and (h), and 16 V (c), (f), and (i); for a three distinct initial radial inter-electrode gap (IR-IEG) distance: (a)–(c) 20 μm, (d)–(f) 40 μm, and (g)–(i) 60 μm.

the entrance side of the hole. However, this difference in the anodic dissolution rate diminishes as the post-processing time progresses. The radial gap at the exit end of the hole enlarges faster than at the entry end because this end is subject to a higher dissolution rate, and as time passes, this end tends to be as wide as the entrance side.

It is also evident from the predicted evolution of the hole profile shown in Figs. 9a and 9i, corresponding to the post-processing time of 7 s and onwards. Surprisingly, at about t = 8 s, practically the whole periphery of the hole becomes an area of low current density, with the current density being less than or equal to the minimum current density (i.e., $J \leqslant J_{\min} = 30$ A cm^2). As a result of the passivation of the anode surface in the presence of passivating sodium nitrate ($NaNO_3$) electrolyte solution, the material dissolving phenomenon terminates.

Furthermore, it can be seen from Figs. 9b–9i that the current density distribution at the entry side is localized near the edge. It is known that the electric field intensity is inversely proportional to the square of the radius of curvature, and since the radius of curvature at the edges is minimum, therefore, the highest of electric field intensity is found nearby the edge. Thus, the anode material dissolves at a greater rate in the region near the hole's edge than in any other area. This phenomenon is termed as the "edge rounding effect".

Experimental validation of the numerical model.—The transient model has been experimentally validated. The model's hole profile evolution prediction was tested across several ECPP time lengths. Cutting these treated holes longitudinally traced the hole profiles. Figure 10 shows validation trial results and numerical discrepancies. At 5 s, 10 s, and 15 s, the experimental hole profile matches the predicted one. Results were within 10% error. Figure 11 shows example FE-SEM hole profiles for different ECPP processing

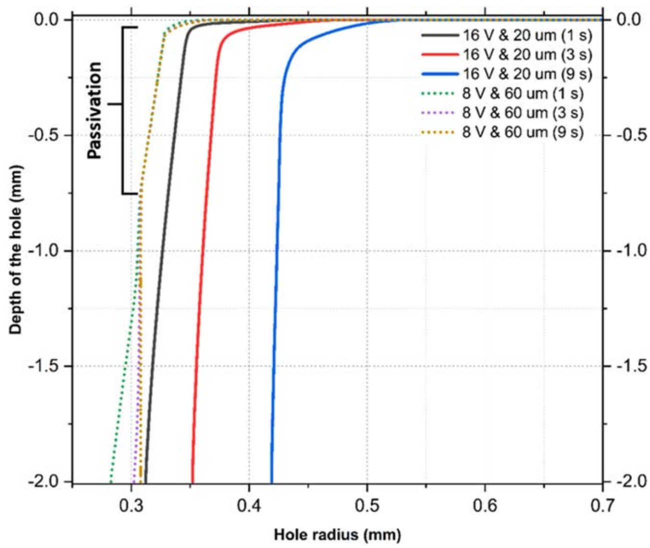

Figure 16. Longitudinal cross-sectional line graphs demonstrating the transient hole profile evolution predicted from simulations performed for two different parametric settings: applied voltage of 16 V and IR-IEG of 20 μm (represented by solid lines) and applied voltage of 8 V and IR-IEG of 60 μm (represented by dotted lines), at t = 1 s, t = 3 s, and t = 9 s.

durations. Figure 11 shows hole entry and exit cross-sectional profiles. The hole profile was circular and thermally unaffected. When ECPP progresses, the material dissolves from the hole wall, enlarging it.

The hole diameters for time steps 10 s and 15 s were practically identical, demonstrating that the material dissolution phenomenon terminates when the minimum current density is reached at the hole perimeter due to the creation of an inert oxide film. The EDX spectrum shown in Fig. 12 reveals the presence of titanium and oxygen only. From the notable absence of tungsten, it can be inferred that the recast layer was completely dissolved. The characteristics of EDM surface features, including micro-cracks, holes, craters, and bumps, were absent. Hence, ECPP improved EDMed hole surface integrity.

Evaluating the performance of ECPP operation: numerical and experimental investigations.—The operating performance of ECPP has been evaluated based on radial hole overcut and mean roughness. The following subsections examine how the performance of the ECPP process changes because of varying process parameters.

Effect on Hole over-cut (HOC).—The applied voltage is an essential process parameter that governs the material dissolution during the electrochemical processing.[35] Besides, the strength and spread of the electric field during ECPP operation are strongly dependent on the IR-IEG value.[36] Therefore, the HOC is also influenced by variations in voltage and IR-IEG. The applied voltage was varied from 8 V to 16 V for three distinct IR-IEG widths of 20 μm, 40 μm, and 60 μm. The IR-IEG was varied by reducing the size of the tool electrode using the in situ wire-EDG process.

The HOC's dependence on the applied voltage for distinct IR-IEG distances is shown in Fig. 13. For a fixed IR-IEG width of 60 μm, the HOC increased by approximately 102% from 80 μm to 162 μm on increasing the applied voltage from 8 V to 16 V. In contrast, it increased by around 111% from 83 μm to 175 μm, and 125% from 102 μm to 230 μm, for 40 μm and 20 μm, respectively, on increasing the applied voltage from 8 V to 16 V. It can be observed from Fig. 13 that the amount of increase in overcutting was larger when the voltage was increased from 14 V to 16 V compared to that for the 8 V to 14 V, for IR-IEG width of 20 μm. The applied voltage of 16 V and the IR-IEG width of 20 μm produced the largest HOC. Greater applied voltages and smaller IR-IEG widths resulted in higher HOC values. At the same time, the smallest HOC was observed, corresponding to the applied voltage of 8 V and IR-IEG of 60 μm.

Figure 14 depicts the typical FE-SEM images of the radial cross-section of the micro-holes.

The edge of micro-holes corresponding to the 8 V and 60 μm parametric setting embraced the perforated recast layer on its peripheral edge. On the contrary, the micro-holes related to the 16 V and 20 μm parametric setting revealed a non-circular edge and a higher spread of stray dissolution. It was observed that the extent of stray dissolution increased with increasing the applied voltage and decreasing IR-IEG. The specific parametric setting (16 V and 20 μm) creates conditions conducive to faster material removal by establishing the highest local current density due to the maximum voltage and minimum initial radial IEG. Consequently, material removal is maximized, leading to the observed higher overcut. Additionally, elevated current density can induce side reactions in the electrochemical process, causing non-uniform material removal. These side reactions may involve gas evolution, changes in local pH, or other factors affecting machining precision.[7] Regions experiencing sustained high current density may undergo more aggressive dissolution, resulting in irregularities in the hole's shape. As a consequence, the achieved dimensional accuracy differed from the expected outcome.

Transient simulations for different parametric settings have also been performed to understand the evolution of hole profile with ECPP duration for varied process parameters. The simulation results concur with experimentally obtained HOC values for corresponding parametric settings. Figure 15 displays the simulation results in the form of radial cross-sectional line graphs for enunciating the time-dependent evolution of the hole profile for various parametric settings. The transient profile evolution suggests that as time passes, the radial-IEG enlarges. Thereby the extent of radial over-cut is progressing away from the longitudinal axis. As time progresses, the current density at the periphery decreases with expanding radial-IEG and eventually attains the minimum current density (J_{min}) value. The anodic dissolution ceases once the current density at the hole periphery reaches the J_{min}.

Ohm's law states that the current is directly proportional to the voltage difference across the IEG. Therefore, an increase in the applied voltage increases the amount of current flowing through the IEG. Combining it with Faraday's law implies that the higher the applied voltage value, the greater the material removal from the anode. The higher applied voltage can shorten the post-processing duration, increasing throughput. However, it also has some adverse effects in terms of higher stray cutting and uncontrolled material dissolution, causing deteriorated dimensional accuracy of micro-holes and surface morphology. Likewise, from Ohm's law, when the IEG is broadened, the electrolyte's ohmic resistance in the IEG increases, raising the voltage drop across the IEG. The current density in the radial direction at the hole's peripheral surface also drops, and consequently, the rate of anodic dissolution slows as per Faraday's law. Therefore, narrower IR-IEG is desired; however, replenishment of fresh electrolytes becomes problematic when the IEG becomes too narrow. Although a wider IEG can facilitate easier replenishment of fresh electrolytes, a wider IEG implies a more considerable voltage drop, thus dissolving lesser anode material.

Consequently, the largest HOC was observed for an applied voltage of 16 V and an IR-IEG of 20 μm, while the smallest values of HOC were observed for an applied voltage of 8 V and an IR-IEG of 60 μm. It can be inferred from radial cross-sectional line graphs shown in Fig. 15 corresponding to the parametric setting of 8 V and 60 μm that the electrochemical dissolution does not occur at the entry side of the hole for all time steps. Therefore, the HOC remains that of the initial EDMed hole, which is around 80 μm. Even at the exit side of the hole, the dissolution stops occurring beyond $t = 3$ s.

On the contrary, for the parametric setting of 16 V and 20 μm, the extent of electrochemical dissolution is greatest at the entry side of the

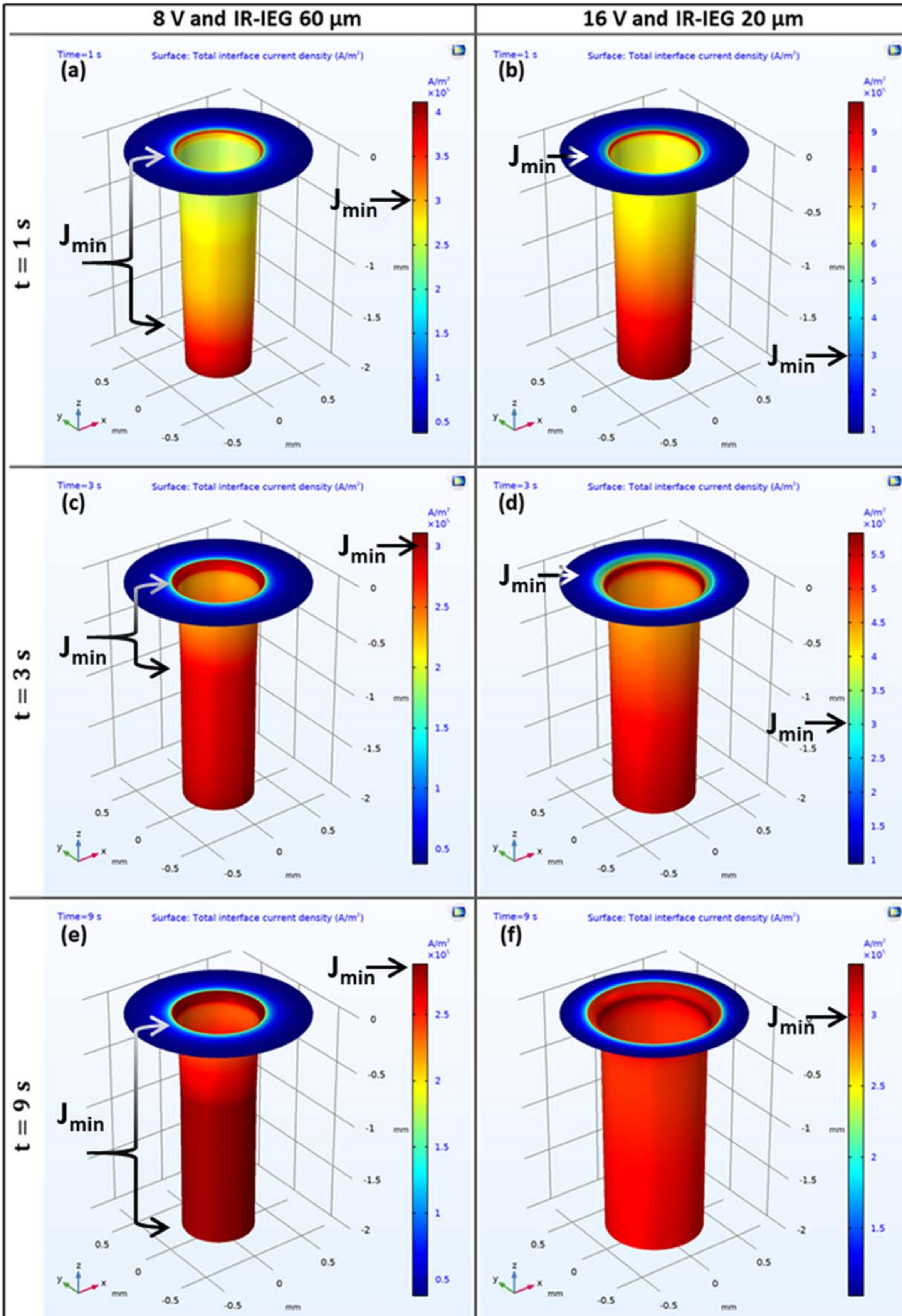

Figure 17. The three-dimensional (3D) shape evolution of the micro-hole and corresponding total current density distribution at the hole surface during ECPP operation performed for t = 1 s (a)–(b), t = 3 s (c)–(d), and t = 9 s (e)–(f) at two parametric settings: applied voltage and IR-IEG of 8 V and 60 μm (a), (c), and (e) and 16 V and 20 μm (b), (d), and (f).

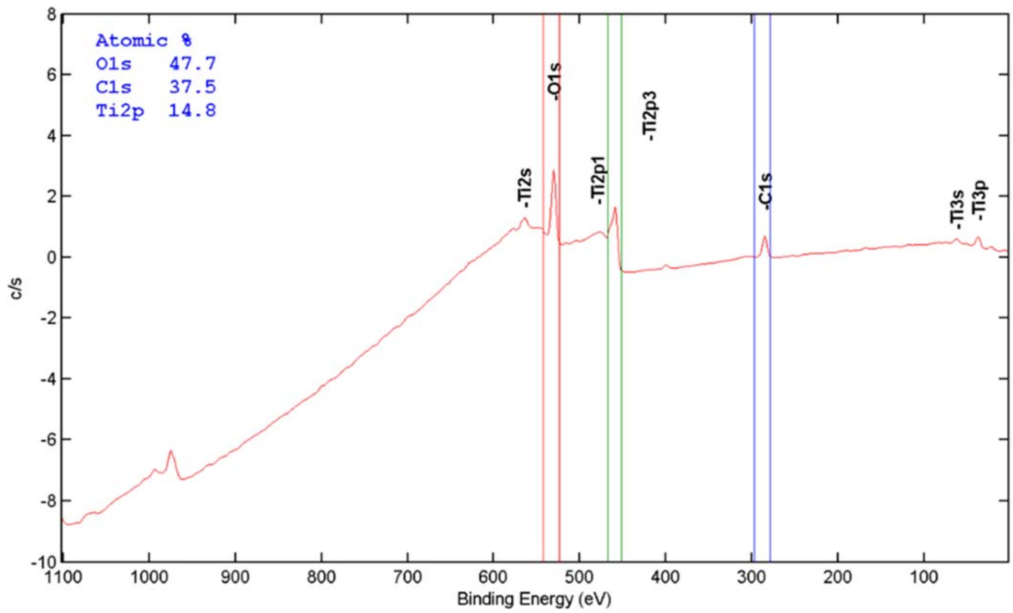

Figure 18. The typical XPS survey spectra correspond to the parametric settings: Voltage (8 V) and IR-IEG (60 μm).

hole. The hole profile evolution stops simultaneously at both entry and exit sides around $t = 9$ s. Figure 16 presents the profile evolution corresponding to these two parametric settings at three distinct periods, i.e., $t = 1$ s, $t = 3$ s, and $t = 9$ s. It can be seen from the figure that the extent of electrochemical dissolution corresponding to the 8 V and 60 μm is far less compared to that at 16 V and 20 μm. Analyzing the distribution of current density at the hole's peripheral surface can help understand how the hole profile evolves with time in these two parametric settings. Figure 17 shows the three-dimensional (3D) shape evolution of the micro-hole and corresponding total current density distribution on the hole surface during ECPP operation at t = 1 s, t = 3 s, and t = 9 s for these two different parametric settings: applied voltage of 8 V and IR-IEG of 60 μm and applied voltage of 16 V and IR-IEG of 20 μm. As discussed earlier, in the passivating electrolyte solution system like aqueous $NaNO_3$ solution, the anodic dissolution stops occurring when the current density reaches a particular value referred to as the minimum current density (J_{min}).

Interestingly, for an applied voltage of 8 V, although the current density at the exit side of the hole attains the J_{min} value only after the 3 s; however current density at the entry side of the hole as soon as the start of ECPP operation, i.e., $t = 1$ s, is already below the minimal value. It appears that the ECPP action at a low value of applied voltages (i.e., 8 V) for an IR-IEG width of 60 μm is not just adequate to dissolve the thermally damaged material from the wall of the hole, refer to Fig. 17a. Therefore, the recast layer cannot be entirely removed at the entry side of the hole at 8 V, corresponding to these conditions, as confirmed from the FE-SEM micrograph shown in Fig. 14k. Thus, the HOC remains that of the initial EDMed hole, around 80 μm. On the other hand, the current density at the entry side of the hole is too strong for a high value of applied voltage (i.e., 16 V) for narrow IR-IEG width (i.e., 20 μm). It results in a considerable extent of HOC and stray dissolution, as evident in the FE-SEM micrograph shown in Fig. 14e.

Short circuits appear if the IEG is narrower than 20 μm, which contradicts the ECPP operation's purpose. The occurrence of short circuits liberates heat energy, causing surface degradation and the creation of pits and bumps. It was observed that when the radial IEG is too narrow, the flushing of reaction by-products and subsequent replenishment of fresh electrolyte solution becomes difficult. Therefore, the undesired phenomena of electrolyte boiling, or short-circuiting may manifest during the post-processing. The issue of stray dissolution becomes predominating at higher applied voltages for narrow IR-IEG values (as can be seen in Figs. 14e, 15c, and 17d–17f)), which subsequently aggravates machining accuracy and eventually mitigates the effectiveness of the ECPP operation.

Furthermore, XPS investigations were carried out to verify the presence of a passive oxide layer at the specific parameter settings of 8 V and 60 μm. Figure 18 displays the typical XPS survey spectra corresponding to these settings. Oxygen (O), titanium (Ti), and carbon (C) peaks were found on microholes surfaces. The presence of carbon on the sample surface can be attributed to adventitious carbon and was employed for charge correction in the XPS tests. Ti and O peaks suggest that titanium oxides are being formed.[37] Depth profiling analyses for Ti and O were also carried out to determine the variation in elemental concentration with film thickness. The outcomes of the XPS depth profiling analysis of surfaces are shown in Fig. 19.

Effect on mean surface roughness (Sa).—Because of how both processes function, the ECM technique can produce smooth surfaces compared to the EDM process. Ramasawmy and Blunt (2002) employed electrochemical dissolution to remove thermal damage and generate smooth surfaces on steel.[38] However, due to the high resistance of commercially pure titanium to electrochemical dissolution, achieving the appropriate surface quality during the ECPP process is difficult without knowing the underlying local material dissolution mechanisms. The requisite material removal and acceptable surface quality can only be obtained by destroying the passivating oxide film on the titanium surface and exposing the new work surface in the electrolyte for polishing action. The polishing action is strongly influenced by the process parameters, including applied voltage and IR-IEG. Investigating how these parameters affect surface roughness becomes vital for machining micro-holes with better surface integrity during the ECPP process. Figure 20 depicts the relationship of Sa on applied voltage for various IR-IEG distances.

The roughness assessment indicated that after the ECPP operation, the Sa values of the microholes surface decreased for all experiments. As previously detailed in Cross-sectional analysis section, the mean roughness (Sa) of the initial holes produced by EDM was approximately 3.01 ± 0.17 μm, and by comparing with Fig. 20, it can be inferred that a significant reduction in roughness can be achieved following the ECPP operation.

For a fixed IR-IEG, an initial decreasing and subsequently increasing trend in Sa value was seen when the applied voltage

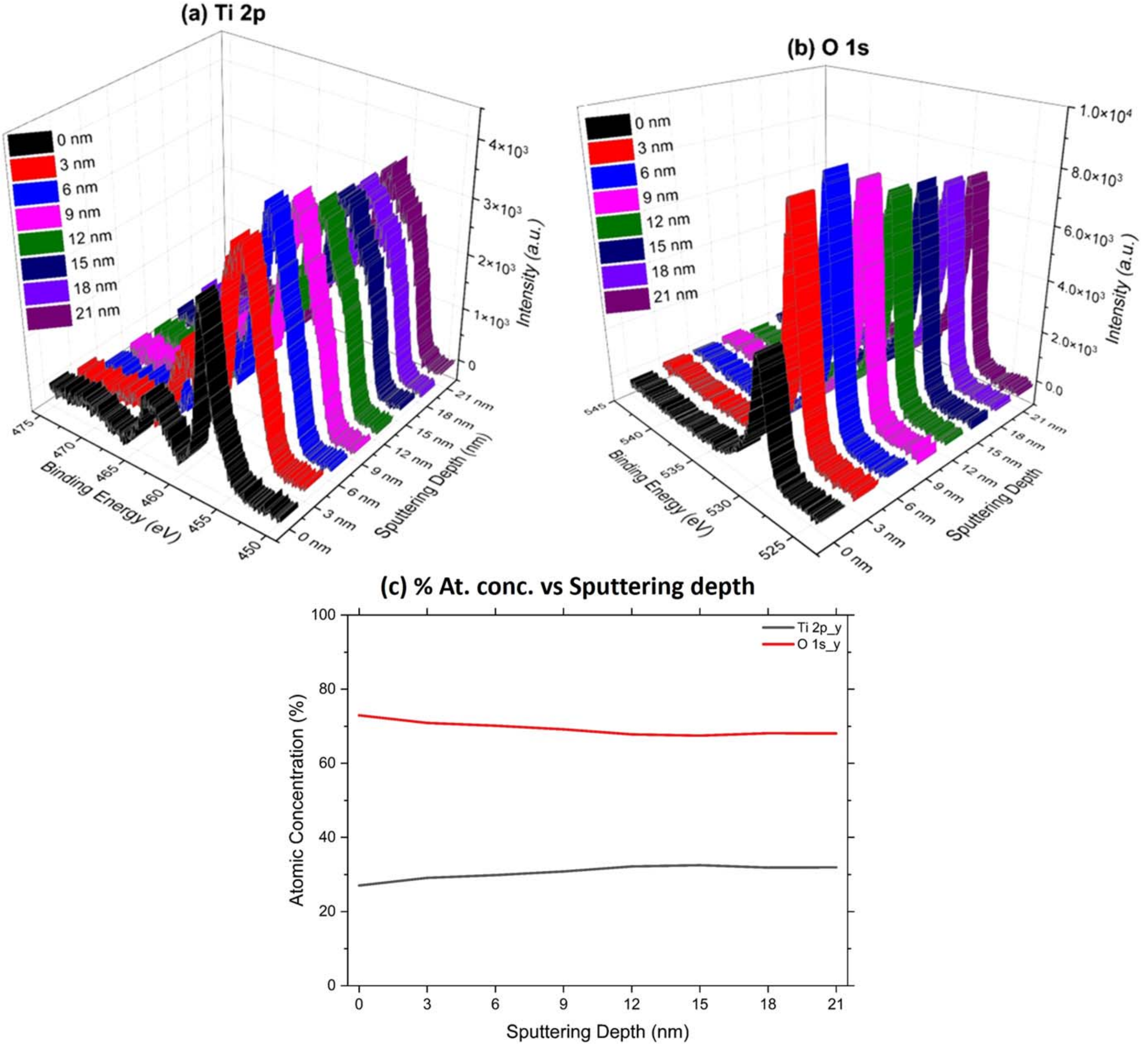

Figure 19. Images showing the typical XPS depth profiling spectra for (a) Ti 2p and (b) O 1 s and (c) the change in atomic concentration with sputtering depth for surfaces treated at parametric settings: Voltage (8 V) and IR-IEG (60 μm).

was increased from 8 V to 12 V and 12 V to 16 V, respectively. For similar applied voltage levels, the lowest Sa values were found for IR-IEG widths of 40 μm and the highest for IR-IEG widths of 20 μm.

Figure 21 displays FE-SEM micrographs representing the surface morphology corresponding to different parametric settings. The traits of the intergranular attack were observed on surfaces processed corresponding to IR-IEG of 20 μm. In contrast, the formation of the passive film and its breakdown were seen on surfaces corresponding to the other IR-IEG widths of 40 μm and 60 μm. It has been previously discussed that as the IR-IEG is widened, the voltage across the IEG drops. It eventually results in a reduction in the overall current density at the hole periphery. Therefore, encouraging a uniform anodic dissolution at the microscopic level because the degree of un-even anodic dissolution caused by severe intergranular attack reduces at lower voltages. Thus, the mean roughness was lower for the IR-IEG distance of 40 μm compared to that of IR-IEG of 20 μm for corresponding values of applied voltages.

However, a higher potential drop associated with 60 μm reduces the intensity of intergranular attack and promotes the formation of passive films by creating regions of low current density. Thereby increasing the chances of the trans-passive anodic dissolution in which the material is dissolved non-uniformly at a microscopic level.[39] Thus, the processed surface becomes rough compared to the IR-IEG of 40 μm. It seems that at the applied voltage of 12 V and IR-IEG of 40 μm, there exists a balance between the inter-granular attack and trans-passive dissolution. As a result, a relatively flat and smooth surface was observed.

For all three values of IR-IEG, an initial increase in the applied voltage to 12 V is thought to enhance the electrochemical polishing action, reducing surface roughness. However, as the applied voltage increases, the strength of the intergranular attack and the trans-passive dissociation phenomenon also increases. Consequently, for applied voltage values above 12 V, these phenomena begin to dominate the electro-polishing activity, leading to a rough surface.

For example, for an IR-IEG of 60 μm, higher applied voltage levels produced rough surfaces. It is well known that two competing

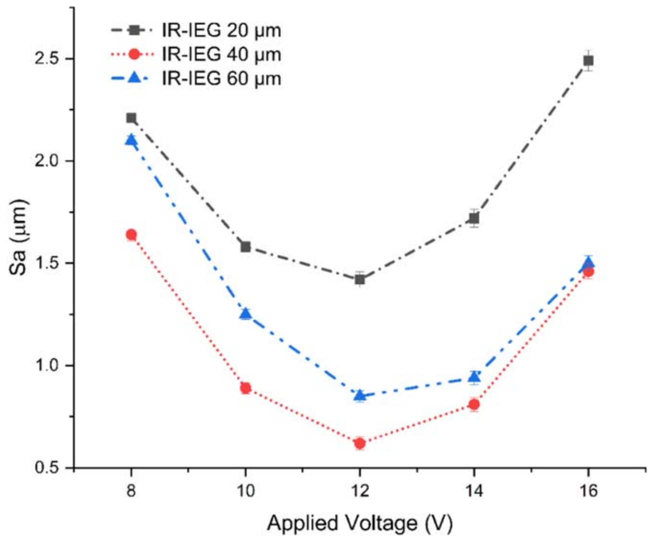

Figure 20. The mean surface roughness for three initial radial inter-electrode gaps (IR-IEG) widths (20, 40, and 60 μm) when the applied voltage is changed from 8 V to 16 V.

phenomena, oxide layer growth and depletion, take place during electrochemical dissolution. Which phenomenon is most prevalent will depend on the local electrochemical conditions. The values of applied voltage and IEG affect the local conditions. Relatively inert titanium oxides form on the surface because of oxidation in low current density zones in the presence of passivating electrolyte solutions. However, the electrolyte gradually attacks this oxide layer through faulty sites, attempting to deplete the layer and resulting in the trans-passive dissolution of work material. The intensity of anion attacks on the passive film increases, increasing the applied voltage. Therefore, the destruction of passive films can be attributed to the rougher surface corresponding to the 60 μm of IR-IEG for higher values of applied voltages, as can be confirmed from FE-SEM micrographs displayed in Figs. 21k–21o.

The sample surfaces processed at higher values of applied voltages (from 12 V to 16 V) embraced the traits of trans-passive dissolution caused by the destruction of the oxide layer. The cracks on the oxide film cause breakage of the passive film and thus lead to uneven anodic dissolution and make the surface relatively rough compared to the low values of applied voltage where the passive film is rather thin and intact.

For IR-IEG of 20 μm, the electrochemical polishing of EDM craters and aggressive intergranular dissolving can be the sources of the initial reducing and subsequent increasing trend in mean roughness with increasing applied voltage, respectively. The residual EDM crater features were absent on the surface, corresponding to the applied voltage of 8 V and IR-IEG of 20 μm. The electrochemical polishing action improved with an initial increase in applied voltage; therefore, reduced Sa values were obtained. Whereas the marks of uneven anodic dissolution caused due to aggressive intergranular attack were observed when the applied voltage was increased beyond 12 V. Thus, this preferred material dissolution at the grain boundaries (inter-granular attack) renders the rough surface morphology corresponding to higher applied voltages compared to that for lower voltages, refer to Figs. 21a–21e.

The surface morphology corresponding to the 40 μm of IR-IEG was observed to be relatively smooth compared to the other two IR-IEG widths for corresponding values of applied voltages. Relatively flat and smooth surface morphology was observed for the applied voltage of 12 V and IR-IEG width of 40 μm.

Expounding the mechanics of the sequential ECPP approach.—The underlying mechanics of the sequential ECPP process may now be established. The goal of the ECPP approach was to produce micro-holes with excellent surface integrity (low surface roughness and devoid of thermal damages such as recast layer) and form precision (almost cylindrical holes) that could not be accomplished with the EDM process alone. Figure 22 displays the schematics illustrating the mechanics of forming smooth, almost cylindrical micro-holes without thermal damages using the in situ sequential ECPP approach. As shown in Fig. 22, the original EDMed holes exhibited two types of nonconformities: surface imperfections and form inaccuracy. Surface imperfections, including the recast layer and the rough surface, can be counted among the phenomena that are uniformly reduced when electrochemical polishing actions are performed, which are usually expected. However, correcting the form inaccuracy of the tapered hole wall was found to be intriguing and can be explained by different rates of material dissolution on the entry and exit sides and the passivation manifestation at different moments of ECPP time.

Although the electrochemical polishing activity is predicted to occur on the entire hole periphery, the material dissolves faster on the tool exit side of the hole, where the initial radial IEG value was the shortest. As the ECPP progresses, the radial IEG expands, resulting in a decrease in the local current density at the hole surface. When the instantaneous radial IEG expands to the point where the local current density approaches the minimum current density (Jmin), further material dissolving stops because a passive oxide layer is formed. Since the initial radial IEG was bigger on the entrance side than on the exit side, the hole's current density reaches the Jmin value faster on the entrance side than on the exit side for a given parametric setting. Thus, the phenomenon of passivation manifests sooner on the entry side than on the exit side. Consequently, material dissolving ceases on the entry side and continues on the exit side, rectifying the initial EDMed hole's geometrical form inaccuracy (tapered wall). This was required to remove the excess material that had to be removed to fix the tapered hole wall. With further progress in anodic dissolution activity at the exit side, the instantaneous radial IEG approaches the IEG value corresponding to minimal local current density (J_{min}), the passivation phenomena also manifest on the exit side of the hole, and the anodic dissolution does not occur further. As a result of the J_{min}, the radial IEG at both the entrance and exit sides becomes almost comparable. Hence, the tapered hole walls become nearly parallel, indicating a decrease in hole taper and an increase in hole form accuracy.

Conclusions

In-situ sequential approach combines EDM with electrochemical post-processing (ECPP) in a sequential manner. The EDM produces initial micro-holes, while the ECPP dissolves thermal damage and corrects form inaccuracies. Instead of experimental research, numerical simulations with experimental investigations have been employed to predict material removal transient behavior and analyze process parameter effects more accurately. Key findings from numerical simulation and experimental investigations include:

- This research has successfully addressed the persistent issue of cross-fluid contamination in the in situ sequential EDM and ECM process by introducing a two-phase dielectric medium (water in air) in the EDM process. This enhancement now positions the approach as more suitable for industrial applications.
- A transient numerical simulation model has been built to predict the evolution of the hole profile during the ECPP operation of initial EDMed micro-holes. The predicted hole profile and the profile obtained from experimental analysis of sectioned micro-holes concurred.
- The X-rays photoelectron spectroscopy (XPS) analysis revealed the formation of passive oxide film on the titanium surface during the processing. Therefore, the phenomenon of passive film formation is also considered to improve the model accuracy.

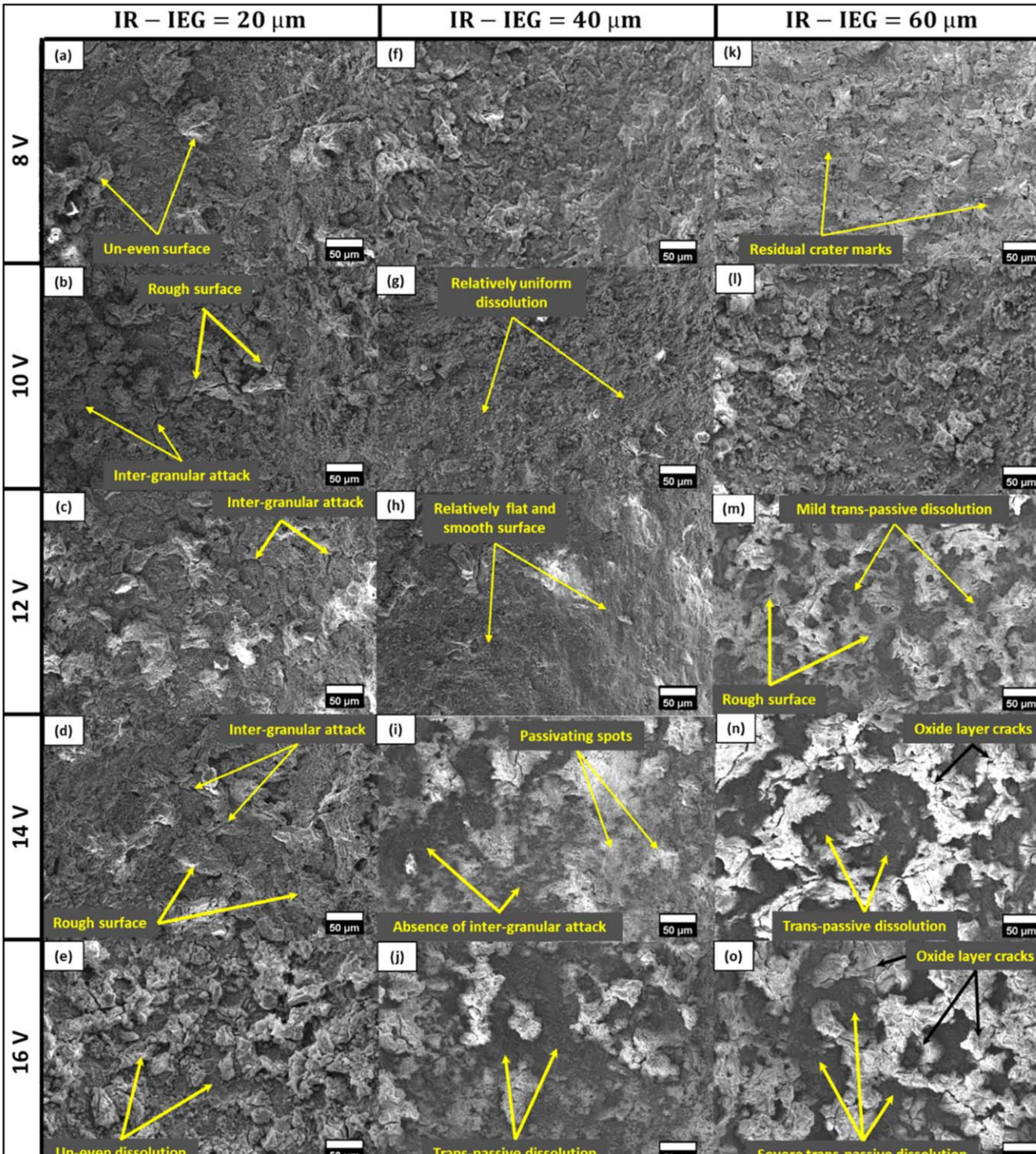

Figure 21. The typical FE-SEM micrographs display the surface morphology of micro-holes. Left to right, the micrographs have 20 μm, 40 μm, and 60 μm initial radial inter-electrode gap (IR-IEG) distances. From 8 V to 16 V, the micrographs are grouped in rows. 50 μm scale bars.

- The ECPP process machined holes with better surface integrity than EDM. Thermally damaged zone, including the recast layer and heat-affected zone, were completely dissolved under most of the tested parameters. The initial holes had an RCL thickness of around 30 μm, which completely dissolved as the material dissolved from the hole periphery under most of the experimental conditions was greater than 80 μm. The ECPPed holes had a mean roughness of 0.61 ± 0.09 μm, approximately 80% lower mean roughness than the EDM holes (3.01 ± 0.17 μm).
- The applied voltage and initial radial inter-electrode gap (IR-IEG) affect the process performance. An IR-IEG width of 20 μm and 60 μm rendered the highest and least radial hole over-cut (HOC) for corresponding values of applied voltages. The HOC grows on increasing the applied voltage for a fixed IR-IEG.
- For similar applied voltage levels, IR-IEG widths of 40 μm had the lowest Sa values, while IR-IEG widths of 20 μm had the highest. For a given IR-IEG, the mean roughness (Sa) reduces as the applied voltage is raised from 8 V to 12 V and subsequently increases when

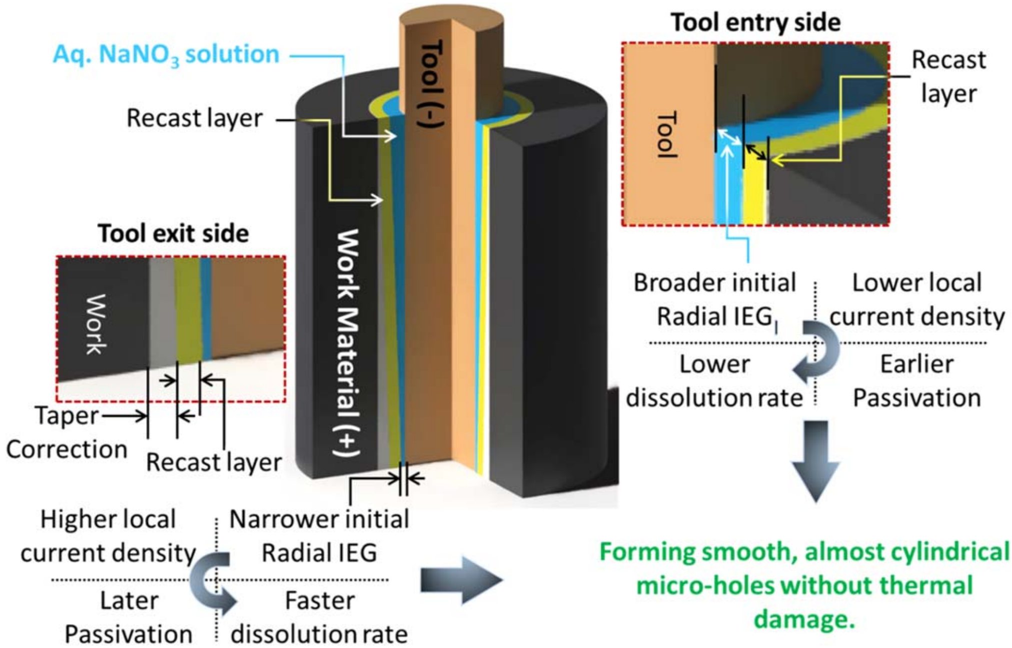

Figure 22. Schematic shows the mechanics of forming smooth, almost cylindrical micro-holes without thermal damage using the in situ sequential ECPP approach.

the voltage is raised over 12 V. For narrow IR-IEG, the characteristics of severe intergranular assault were seen at higher applied voltages. In the case of wide IR-IEG, trans-passive disintegration was observed. It implies that at 12 V applied voltage and 40 μm IR-IEG, a balance exists between inter-granular assault and trans-passive dissolution. As a result, the surface was reasonably flat and smooth.

Understanding the material dissolution activities that occur during the ECPP process revealed by this transient simulation model will assist in manufacturing micro-holes of predetermined diameters without the need to conduct experiments. It can be used in controlling the dimensional accuracy of the ECPP operation. Determining the evolution of hole profiles via experimentation entails using experimental resources and micro-hole cross-sectioning to trace the hole profiles. Cross-sectioning micro-holes is a complex and costly process that necessitates precise cross-sectioning equipment. Thereby, this research enables a cost-effective alternative. The developed transient model accurately predicts the evolution of the hole profile. However, further research is needed to predict transient changes in mean roughness values throughout the ECPP process.

Acknowledgments

The authors thank the Science and Engineering Research Board (SERB), Department of Science and Technology (DST), Government of India, for providing partial financial support under the grant code CRG/2018/004396.

ORCID

Ramver Singh https://orcid.org/0000-0002-9756-4093

References

1. L. Urtekin, F. Bozkurt, H. B. Özerkan, C. Çoğun, and İ. Uslan, “The comparison of performance of electrolytic Cu and CuBe tool electrodes in electric discharge machining of Ti6Al4V alloy.” *El-Cezeri J. Sci. Eng.*, **8**, 1455 (2021), http://hdl.handle.net/20.500.12416/6107.
2. B. He, D. Wang, J. Zhang, and W. Lei, “Investigation of electrochemical dissolution behavior of near-α TA15 titanium alloy in NaCl solution with low-frequency pulse current.” *J. Electrochem. Soc.*, **169**, 043515 (2022).
3. W. Liu et al., “Effect of anodic behavior on electrochemical machining of TB6 titanium alloy.” *Electrochim. Acta*, **233**, 190 (2017).
4. Q. Mohsen and S. A. Fadl-Allah, “Improvement in corrosion resistance of commercial pure titanium for the enhancement of its biocompatibility.” *Mater. Corros.*, **62**, 310 (2011).
5. E. O. Ezugwu and Z. M. Wang, “Titanium alloys and their machinability.” *J. Mater. Process. Technol.*, **68**, 262 (1997).
6. H. B. Özerkan and C. Çoğun, “Electrochemical small diameter deep hole drilling of powder metal steel.” *Trans. FAMENA*, **44**, 47 (2021).
7. A. Vats, R. Singh, A. Dvivedi, and P. Kumar, “Enhancing surface integrity of micro-holes machined on inconel 718 using shaped tube electrochemical machining via hydroxide mixing.” *J. Electrochem. Soc.*, **170**, 113504 (2023).
8. R. Singh, A. Dvivedi, and P. Kumar, “EDM of high aspect ratio micro-holes on Ti-6Al-4V alloy by synchronizing energy interactions.” *Mater. Manuf. Process.*, **35**, 1188 (2020).
9. T. Tiwari, A. Dvivedi, and P. Kumar, “On application of tool mimic approach for fabrication of functional surfaces using EDM process.” *J. Brazilian Soc. Mech. Sci. Eng.*, **45**, 190 (2023).
10. A. la Monaca et al., “Surface integrity in metal machining - Part II: functional performance.” *Int. J. Mach. Tools Manuf.*, **164**, 103718 (2021).
11. D. Novovic, R. C. Dewes, D. K. Aspinwall, W. Voice, and P. Bowen, “The effect of machined topography and integrity on fatigue life.” *Int. J. Mach. Tools Manuf.*, **44**, 125 (2004).
12. R. Singh, A. Dvivedi, and P. Kumar, “Evaluation of the surface integrity of titanium nitride coating deposited on the Ni–Ti substrate through the near-dry electrical discharge surface coating process.” *TMS 2021 150th Annual Meeting & Exhibition Supplemental Proceedings* (Springer, Berlin) p. 421 (2021).
13. L. Urtekin, H. B. Özerkan, C. Cogun, A. Genc, Z. Esen, and F. Bozkurt, “Experimental investigation on wire electric discharge machining of biodegradable AZ91 Mg alloy.” *J. Mater. Eng. Perform.*, **30**, 7752 (2021).
14. H. B. Özerkan, “Theoretical investigation of the effect of surface roughness on the fatigue life of austenitic stainless steels.” *Mater. Today Proc.*, **11**, 417 (2019).
15. N. Dixit, V. Sharma, and P. Kumar, “Research trends in abrasive flow machining: A systematic review.” *J. Manuf. Process.*, **64**, 1434 (2021).
16. T. Masuzawa, C.-L. Kuo, and M. Fujino, “A combined electrical machining process for micronozzle fabrication.” *CIRP Ann.*, **43**, 189 (1994).
17. L. Xiaowei, J. Zhixin, Z. Jiaqi, and L. Jinchun, “A combined electrical machining process for the production of a flexure hinge.” *J. Mater. Process. Tech.*, **71**, 373 (1997).
18. J. C. Hung, B. H. Yan, H. S. Liu, and H. M. Chow, “Micro-hole machining using micro-EDM combined with electropolishing.” *J. Micromechanics Microengineering*, **16**, 1480 (2006).
19. Z. Zeng, Y. Wang, Z. Wang, D. Shan, and X. He, “A study of micro-EDM and micro-ECM combined milling for 3D metallic micro-structures.” *Precis. Eng.*, **36**, 500 (2012).
20. M. D. Nguyen, M. Rahman, and Y. S. Wong, “Enhanced surface integrity and dimensional accuracy by simultaneous micro-ED/EC milling.” *CIRP Ann. - Manuf. Technol.*, **61**, 191 (2012).
21. T. H. Drake and J. A. McGeough, “Aspects of drilling by electrochemical arc machining.” *Proceedings of the Twenty-second International Machine Tool Design and Research Conference* (Macmillan Education UK, London) p. 361 (1982).

22. D. K. Chung, H. S. Shin, B. H. Kim, M. S. Park, and C. N. Chu, "Surface finishing of micro-EDM holes using de-ionized water." *J. Micromechanics Microengineering*, **19**, 045025 (2009).
23. J. Meng et al., "Experimental investigation on simultaneous machining of EDM and ECM with different electrode materials." *Surf. Topogr.: Metrol. Prop.*, **10**, 045014 (2022).
24. S. Ahmed, A. Speidel, J. W. Murray, N. Ahmed, M. Cuttell, and A. T. Clare, "Electrolytic-dielectrics: a route to zero recast electrical discharge machining." *Int. J. Mach. Tools Manuf*, **181**, 103941 (2022).
25. Ramver, A. Dvivedi, and P. Kumar, "On improvement in surface integrity of μ-EDMed Ti–6Al–4V alloy by μ-ECM process." *TMS 2019 148th Annual Meeting & Exhibition Supplemental Proceedings* (Springer International Publishing Cham, San Antonio) p. 745 (2019).
26. Ramver, V. K. Yadav, P. Kumar, and A. Dvivedi, "Experimental Investigation on Surface Morphology of Micro-EDMed Ti-6Al-4 V Alloy." *Recent Advances in Mechanical Infrastructure, Lecture Notes in Intelligent Transportation and Infrastructure*, ed. A. K. Parwani and P. Ramkumar (Springer Nature Singapore Pte Ltd, IITRAM Ahmedabad) p. 69 (2020).
27. H. B. Özerkan and C. Çoğun, "Design and implementation of an electrode feed rate control system in the electrochemical drilling process." *J. Brazilian Soc. Mech. Sci. Eng.*, **44**, 1 (2022).
28. V. K. Yadav, R. Singh, P. Kumar, and A. Dvivedi, "Investigating the performance of the rotary tool near-dry electrical discharge machining process through debris analysis." *J. Mater. Eng. Perform.*, **31**, 8405 (2022).
29. V. K. Yadav, R. Singh, P. Kumar, and A. Dvivedi, "Performance enhancement of rotary tool near-dry EDM process through tool modification." *J. Brazilian Soc. Mech. Sci. Eng.*, **43**, 72 (2021).
30. R. Kumar and I. Singh, "A modified electrode design for improving process performance of electric discharge drilling." *J. Mater. Process. Technol.*, **264**, 211 (2019).
31. R. Kumar and I. Singh, "Productivity improvement of micro EDM process by improvised tool." *Precis. Eng.*, **51**, 529 (2018).
32. V. K. Yadav, Ramver, P. Kumar, and A. Dvivedi, "Investigation on the effect of input parameters on surface quality during rotary tool near-dry EDM." *Recent Advances in Mechanical Infrastructure, Lecture Notes in Intelligent Transportation and Infrastructure*, ed. A. K. Parwani and P. Ramkumar (Springer, Singapore) p. 41 (2020).
33. A. K. M. De Silva, H. S. J. Altena, and J. A. McGeough, "Precision ECM by process characteristic modelling." *CIRP Ann. - Manuf. Technol.*, **49**, 151 (2000).
34. A. Ntasi, W. D. Mueller, G. Eliades, and S. Zinelis, "The effect of electro discharge machining (EDM) on the corrosion resistance of dental alloys." *Dent. Mater.*, **26**, e237 (2010).
35. A. Gomez-Gallegos, F. Mill, A. R. Mount, S. Duffield, and A. Sherlock, "3D multiphysics model for the simulation of electrochemical machining of stainless steel (SS316)." *Int. J. Adv. Manuf. Technol.*, **95**, 2959 (2018).
36. M. Datta and D. Landolt, "Electrochemical machining under pulsed current conditions." *Electrochim. Acta*, **26**, 899 (1981).
37. Y. Wang, Z. Xu, and A. Zhang, "Anodic characteristics and electrochemical machining of two typical γ-TiAl alloys and its quantitative dissolution model in NaNO3 solution." *Electrochim. Acta*, **331**, 135429 (2020).
38. H. Ramasawmy and L. Blunt, "Effect of EDM process parameters on 3D surface topography." *J. Mater. Process. Technol.*, **148**, 155 (2004).
39. J. L. Trompette, L. Massot, L. Arurault, and S. Fontorbes, "Influence of the anion specificity on the anodic polarization of titanium." *Corros. Sci.*, **53**, 1262 (2011).